SUPPORTING INFORMATION

Anticooperative Self-Assembly of Perylene Diimide Dyes in Water Unveiled by Advanced Molecular Dynamics Simulations

Marta Cantina,[a] Daniele Padula,[b] Alekos Segalina,[c] Samuele Giannini,[d] Fabrizio Santoro,[d] Giacomo Prampolini,*[d] and Mariachiara Pastore*[a]

[a]*Université de Lorraine & CNRS, LPCT*
UMR 7019, F-54000 Nancy, France
[b]*Dipartimento di Biotecnologie, Chimica e Farmacia* (Università di Siena)
via Aldo Moro 2, Siena, SI, Italy
[c]*Center for Advanced Reaction Dynamics* (Institute for Basic Science (IBS)
Daejeon 34141, Republic of Korea ;
Department of Chemistry and KI for the BioCentury (Korea Advanced Institute of Science and Technology (KAIST)
Daejeon 34141, Republic of Korea
[d]*Istituto di Chimica dei Composti OrganoMetallici* (ICCOM-CNR),
Area della Ricerca, via G. Moruzzi 1, I-56124 Pisa, Italy

*mariachiara.pastore@univ-lorraine.fr, giacomo.prampolini@pi.iccom.cnr.it

Contents

A Aggregates and Supramolecular descriptors

A.1 Considered aggregates and molecular reference axes

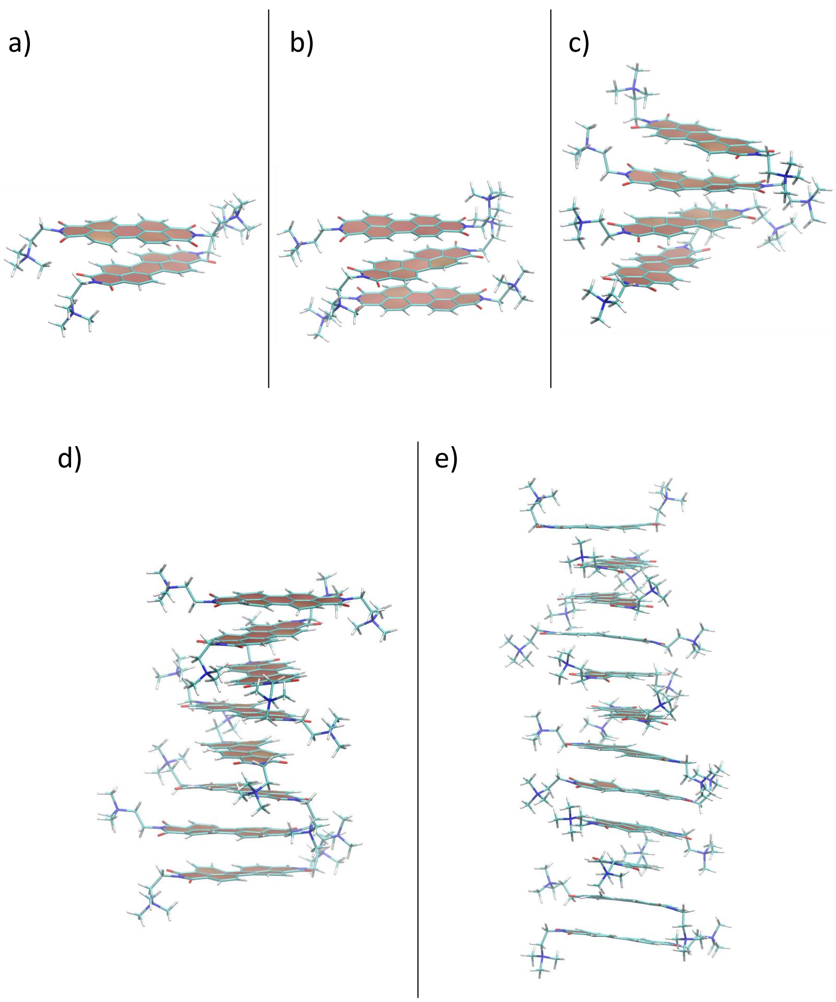

Figure S1: Aggregates considered in this work: (a) $\mathbf{PDI_2}$; (b) $\mathbf{PDI_3}$; (c), $\mathbf{PDI_4}$; (d) $\mathbf{PDI_8}$; (e) $\mathbf{PDI_{12}}$. Each PDI unit k within each aggregate is labeled in alphabetical order from the bottom of the column: k = a, b, c, ...

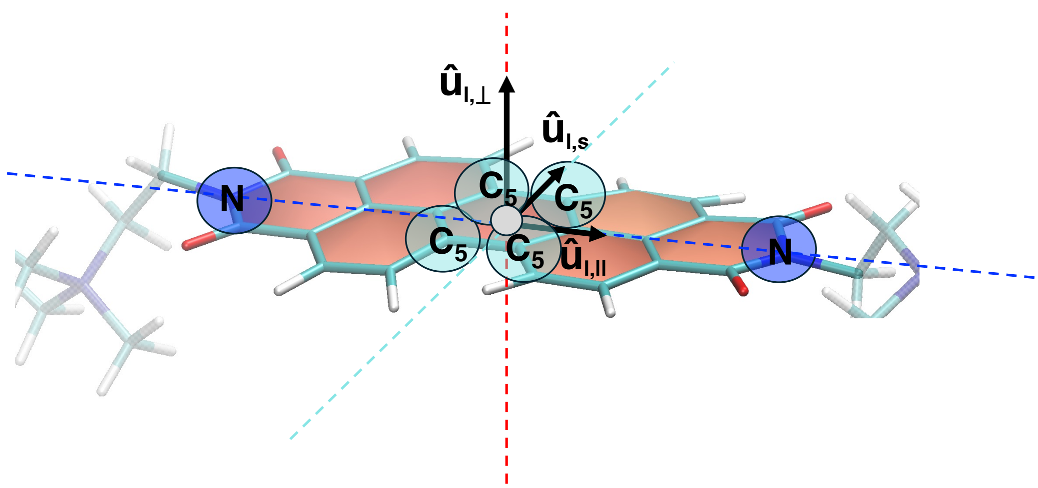

Figure S2: Center of mass (gray sphere), reference molecular axes $\widehat{u}_{k,\|}$ (blue), $\widehat{u}_{k,s}$ (cyan) and $\widehat{u}_{k,\perp}$ (red), and PDI's core atoms used for their definition: Nitrogen (N) and inner Carbon (C_5)

A.2 Supramolecular descriptors

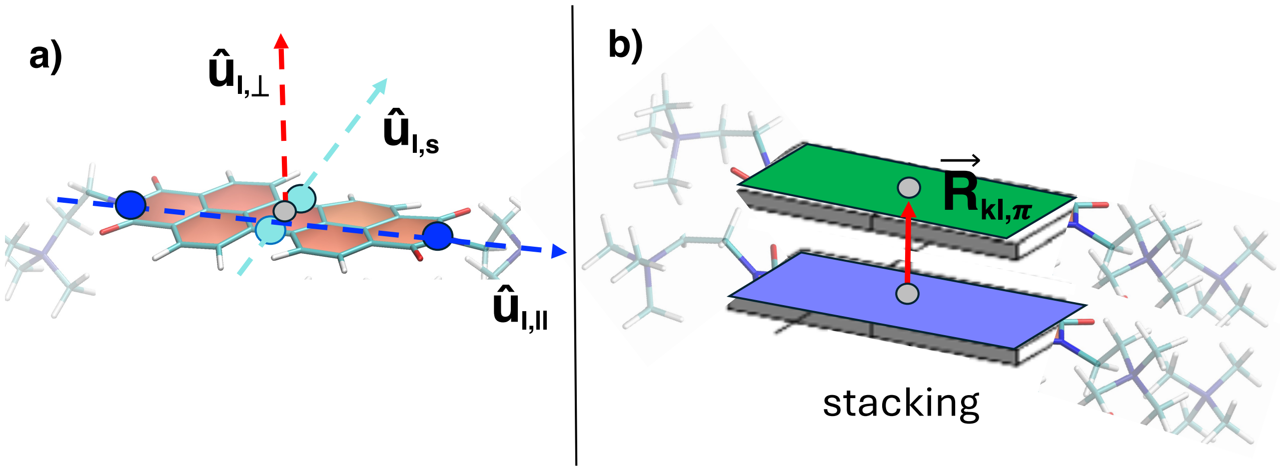

Figure S3: Stacking motion: a) definition of the molecular reference axis on PDI unit k; b) definition of the stacking vector $\vec{R}_{kl,\pi}$ between monomers k (blue) and l (green).

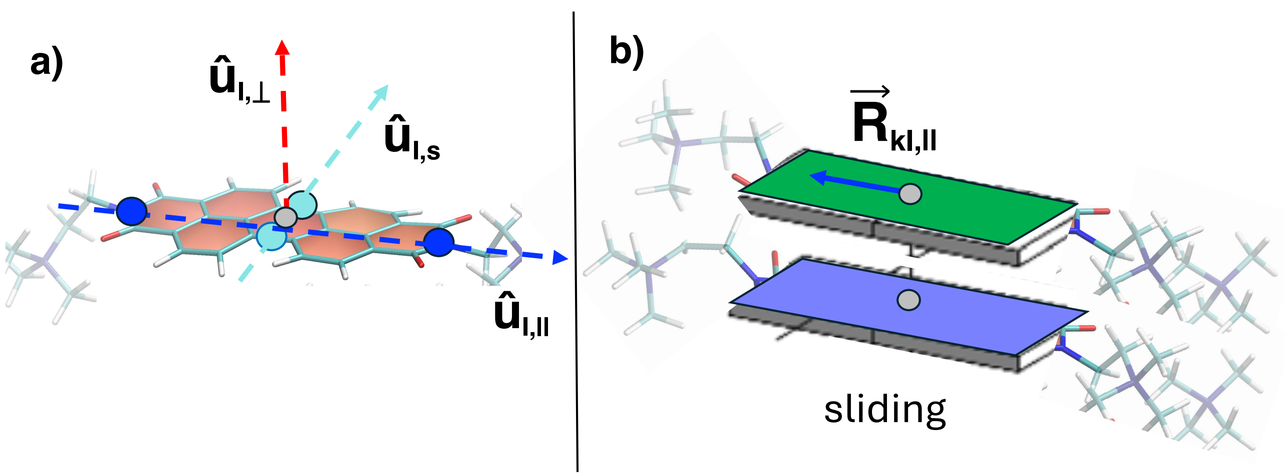

Figure S4: Sliding motion: a) definition of the molecular reference axis on PDI unit k; b) definition of the sliding vector $\vec{R}_{kl,||}$ between monomers k (blue) and l (green).

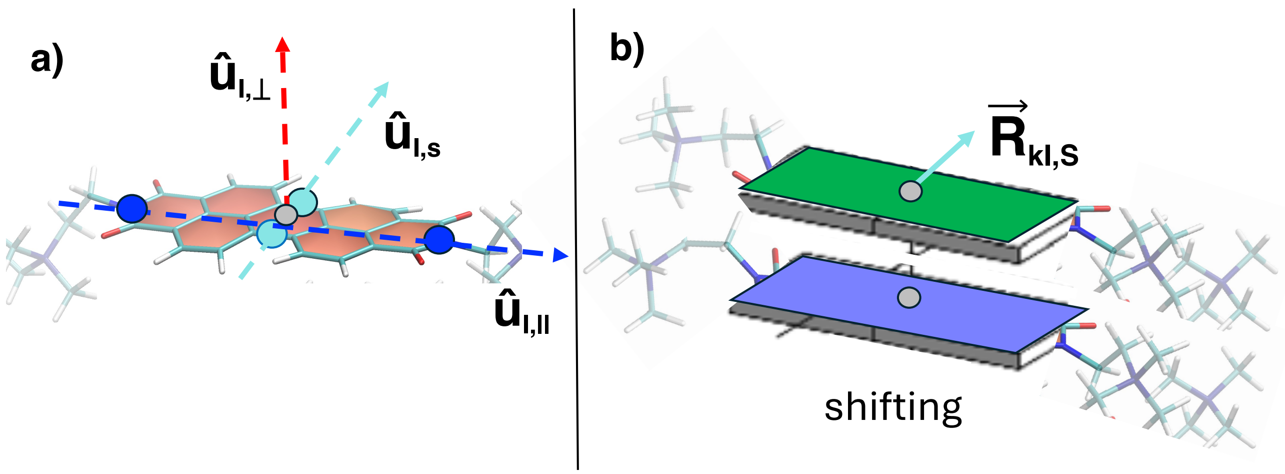

Figure S5: Shifting motion: a) definition of the molecular reference axis on PDI unit k; b) definition of the shifting vector $\vec{R}_{kl,S}$ between monomers k (blue) and l (green).

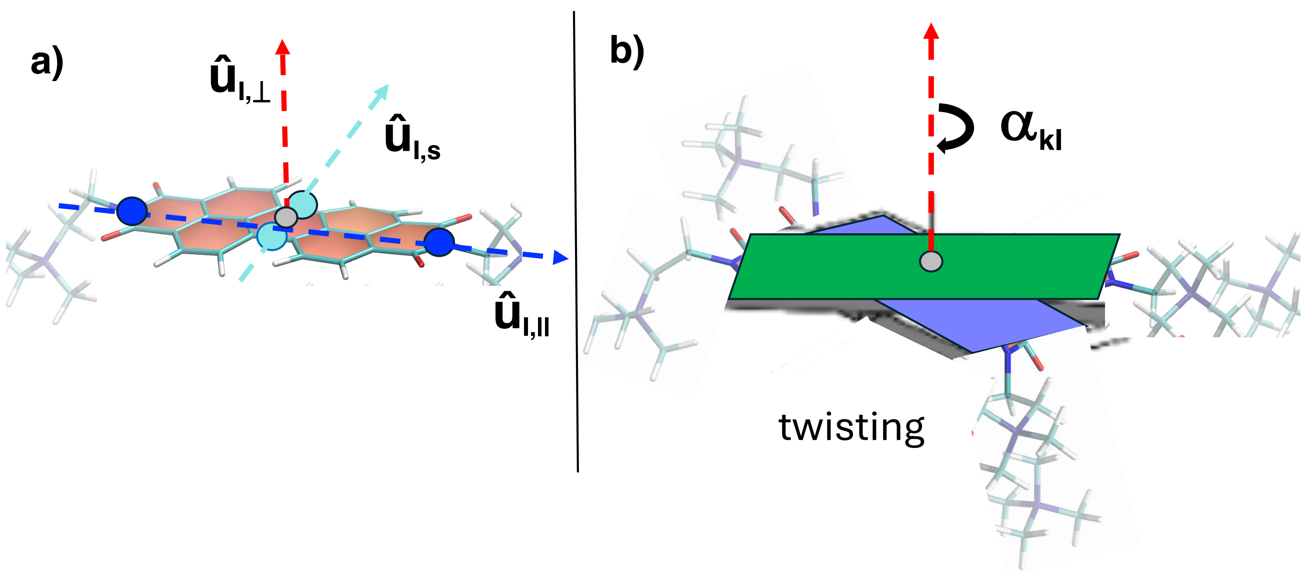

Figure S6: Twisting motion: a) definition of the molecular reference axis on PDI unit k; b) definition of the twisting (yawn) angle α_{kl} between monomers k (blue) and l (green).

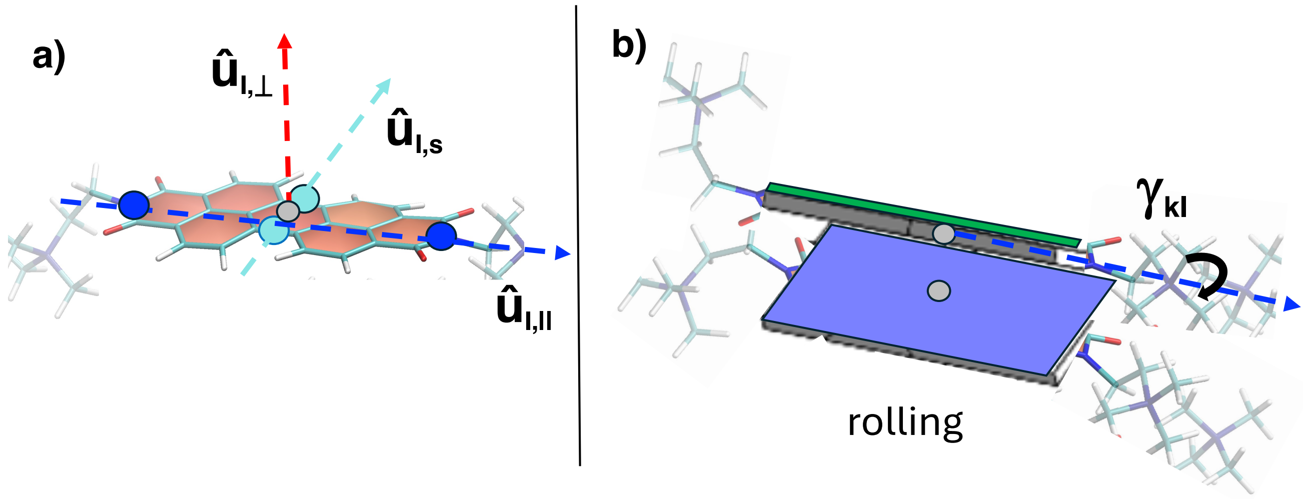

Figure S7: Rolling motion: a) definition of the molecular reference axis on PDI unit k; b) definition of the rolling angle $gamma_{kl}$ between monomers k (blue) and l (green).

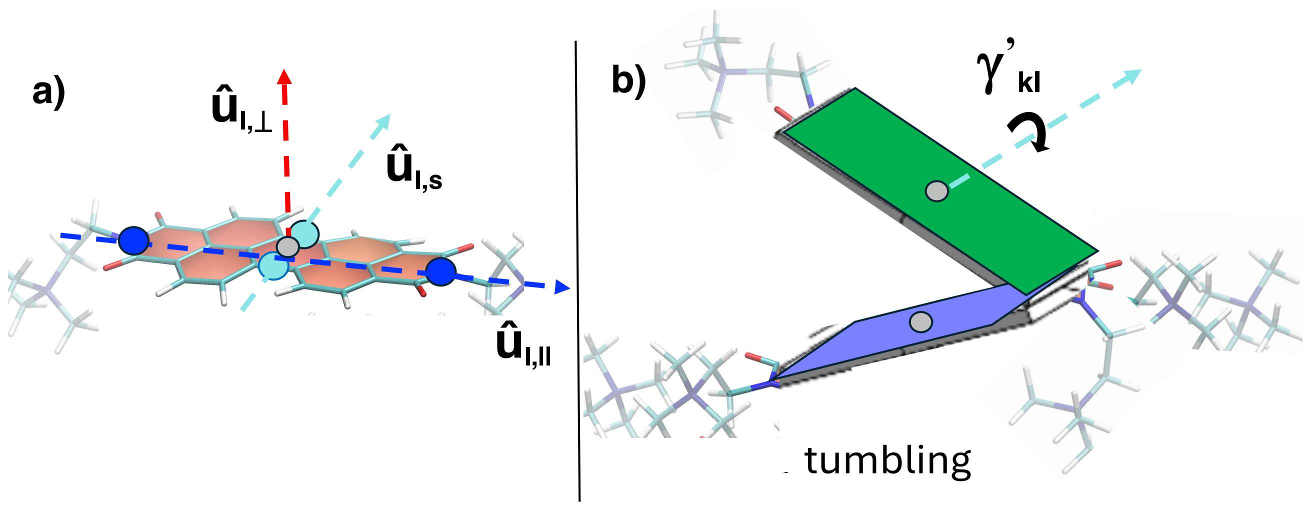

Figure S8: Tumbling motion: a) definition of the molecular reference axis on PDI unit k; b) definition of the tumbling (pitch) angle γ'_{kl} between monomers k (blue) and l (green).

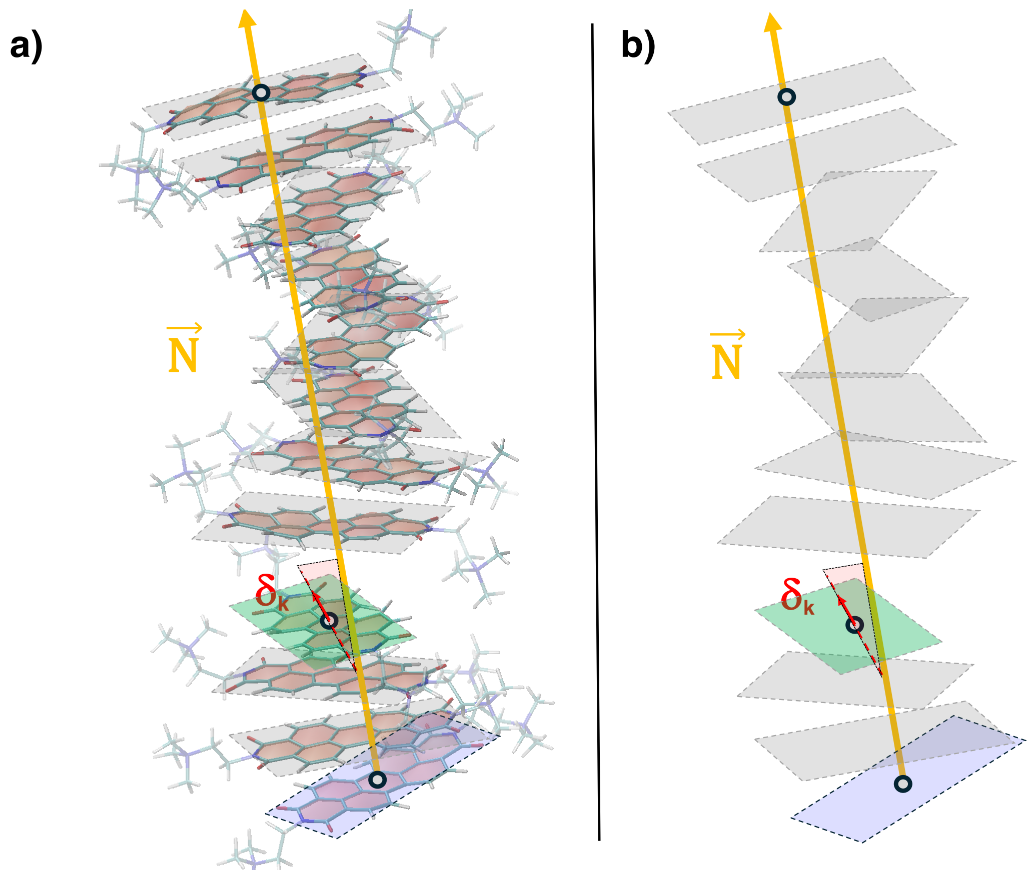

Figure S9: Definition of the columnar vector $\vec{N}$ (orange arrow) and the unit k (green) dephasing angle δ_k for the k PDI unit in an assembled dodecamer. Similar descriptors were assigned for all units in all considered aggregates.

B Self-assembly and supramolecular dynamics

B.1 Self-assembled aggregates

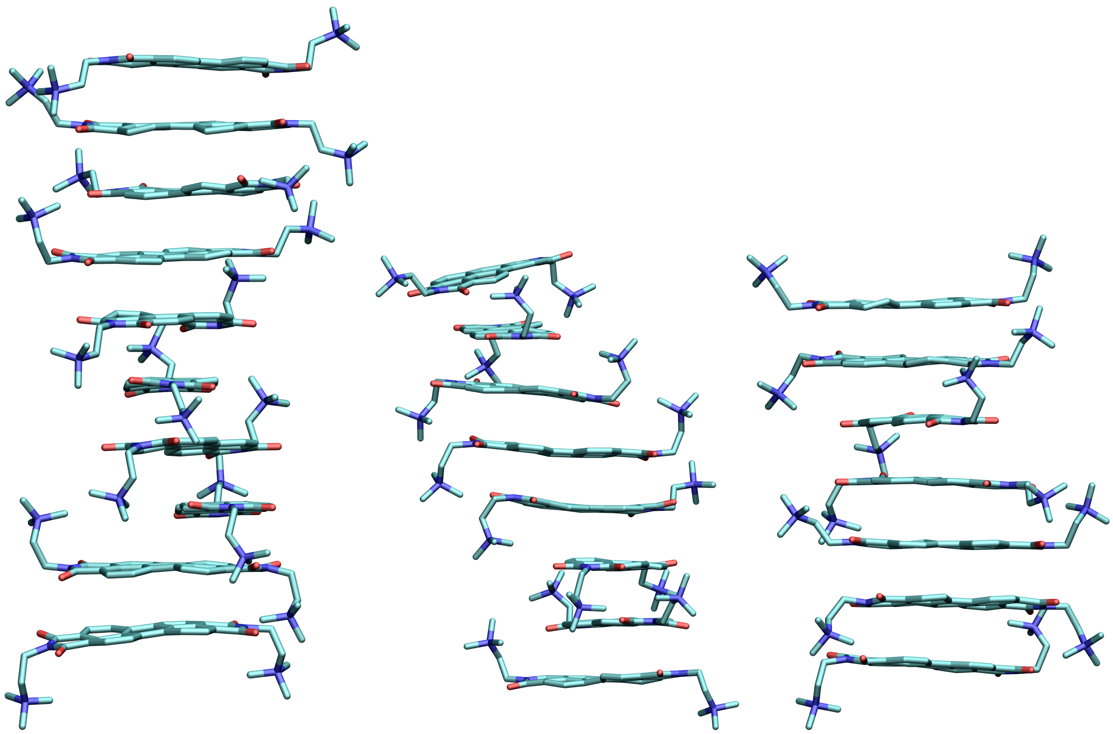

Figure S10: Examples of decamer, octamer and heptamer aggregates obtained from HREMD simulations.

B.2 Binding and interaction energies

Table S1: Calculated binding free energies ΔG ($kJ \cdot mol^{-1}$) for self-assembled aggregates of varied dimensions.

n. of PDIs		**ΔG** ($kJ \cdot mol^{-1}$)
2	**PDI-PDI**	-46.0 ± 2.0
3	**PDI-PDI$_2$**	-41.0 ± 1.8
4	**PDI-PDI$_3$**	-38.0 ± 2.1
4	**PDI$_2$-PDI$_2$**	-40.0 ± 1.9
5	**PDI-PDI$_4$**	-36.6 ± 1.9
5	**PDI$_2$-PDI$_3$**	-37.4 ± 1.8
6	**PDI-PDI$_5$**	-35.5 ± 1.8
6	**PDI$_2$-PDI$_4$**	-37.0 ± 1.7
6	**PDI$_3$-PDI$_3$**	-36.2 ± 2.0

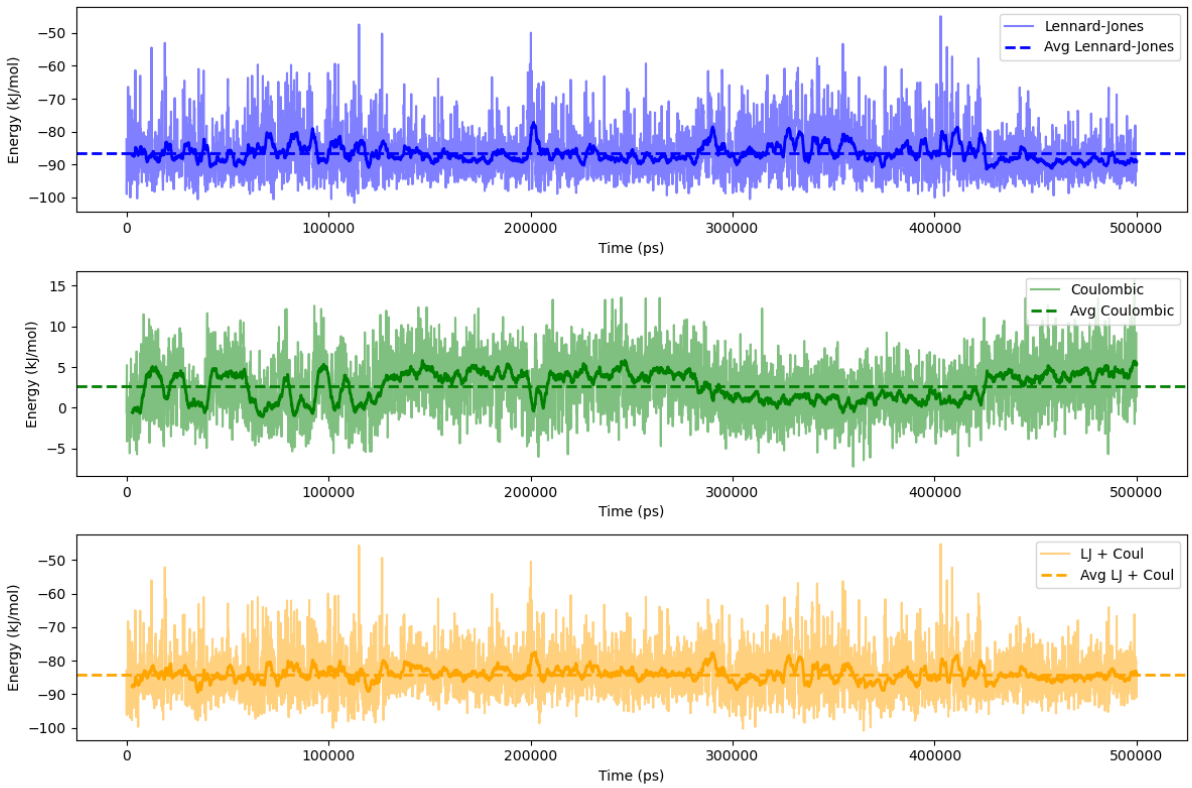

Figure S11: LJ (top, blue) and Coulombic (middle, green) contributions to the total interaction energy ΔE (bottom, orange) between two PDI cores within the inner PDI pair within the aggregate observed in $\mathbf{PDI_8}@H_2O$ simulation. The average value of each data set is reported with dashed line in every panel.

Table S2: LJ and Coulomb contribution to the interaction energy ΔE_{kl} between PDI cores k and l, computed along the MD simulations of $\mathbf{PDI_2}@H_2O$, $\mathbf{PDI_3}@H_20$ and $\mathbf{PDI_4}@H_20$.

Pair	$\mathbf{PDI_2}@H_2O$		$\mathbf{PDI_3}@H_2O$		$\mathbf{PDI_4}@H_2O$	
k-l	LJ (kJ/mol)	Coul (kJ/mol)	LJ (kJ/mol)	Coul (kJ/mol)	LJ (kJ/mol)	Coul (kJ/mol)
a-b	-91.8 ± 5.0	2.5 ± 3.5	-90.0 ± 5.5	2.8 ± 3.3	-89.4 ± 6.3	3.2 ± 3.0
b-c			-89.7 ± 5.4	2.9 ± 3.2	-88.7 ± 5.5	2.4 ± 3.4
c-d					-89.4 ± 6.1	3.2 ± 3.2

Table S3: LJ and Coulomb contribution to the interaction energy ΔE_{kl} between PDI cores k and l, computed along the MD simulations of **PDI$_8$**@H_2O, and **PDI$_{12}$**@H_2O.

Pair	**PDI$_8$@H_2O**		**PDI$_{12}$@H_2O**	
k-l	LJ (kJ/mol)	Coul (kJ/mol)	LJ (kJ/mol)	Coul (kJ/mol)
a-b	-88.7 ± 5.6	2.9 ± 3.4	-89.7 ± 5.7	2.8 ± 3.4
b-c	-86.7 ± 6.6	2.6 ± 3.3	-86.8 ± 6.4	2.5 ± 3.3
c-d	-86.6 ± 7.3	2.4 ± 3.4	-86.5 ± 6.3	2.8 ± 3.3
d-e	-86.7 ± 7.3	2.6 ± 3.5	-86.4 ± 6.7	2.1 ± 3.4
e-f	-86.9 ± 7.2	2.5 ± 3.4	-86.8 ± 6.3	2.5 ± 3.4
g-h	-86.8 ± 6.6	2.6 ± 3.3	-87.3 ± 6.4	3.2 ± 3.3
h-i	-89.0 ± 5.6	3.0 ± 3.3	-87.8 ± 6.6	3.3 ± 3.4
i-j			-87.2 ± 7.0	3.0 ± 3.4
j-k			-86.9 ± 6.5	2.7 ± 3.3
k-l			-86.8 ± 6.5	2.5 ± 3.3
l-m			-89.6 ± 5.7	2.8 ± 3.4

B.3 Supramolecular dynamics

Table S4: Results from Moment Analysis of the Distribution of the distance ρ between PDI cores k and l, computed along the MD simulations of **PDI$_2$**@H_2O and **PDI$_4$**@H_2O. M_1 (Å) represents the normalised first moment, M_2 (Å^2) is the second moment, and σ (Å) corresponds to the standard deviation of the distributions.

Pair	**PDI$_2$@H_2O**			**PDI$_4$@H_2O**		
k-l	M_1 (Å)	M_2 (Å^2)	σ (Å)	M_1 (Å)	M_2 (Å^2)	σ (Å)
a-b	4.12	17.08	0.34	3.87	15.05	0.26
b-c				3.95	15.70	0.32
c-d				3.90	15.28	0.28

B.3.1 Translational dynamics

Stacking

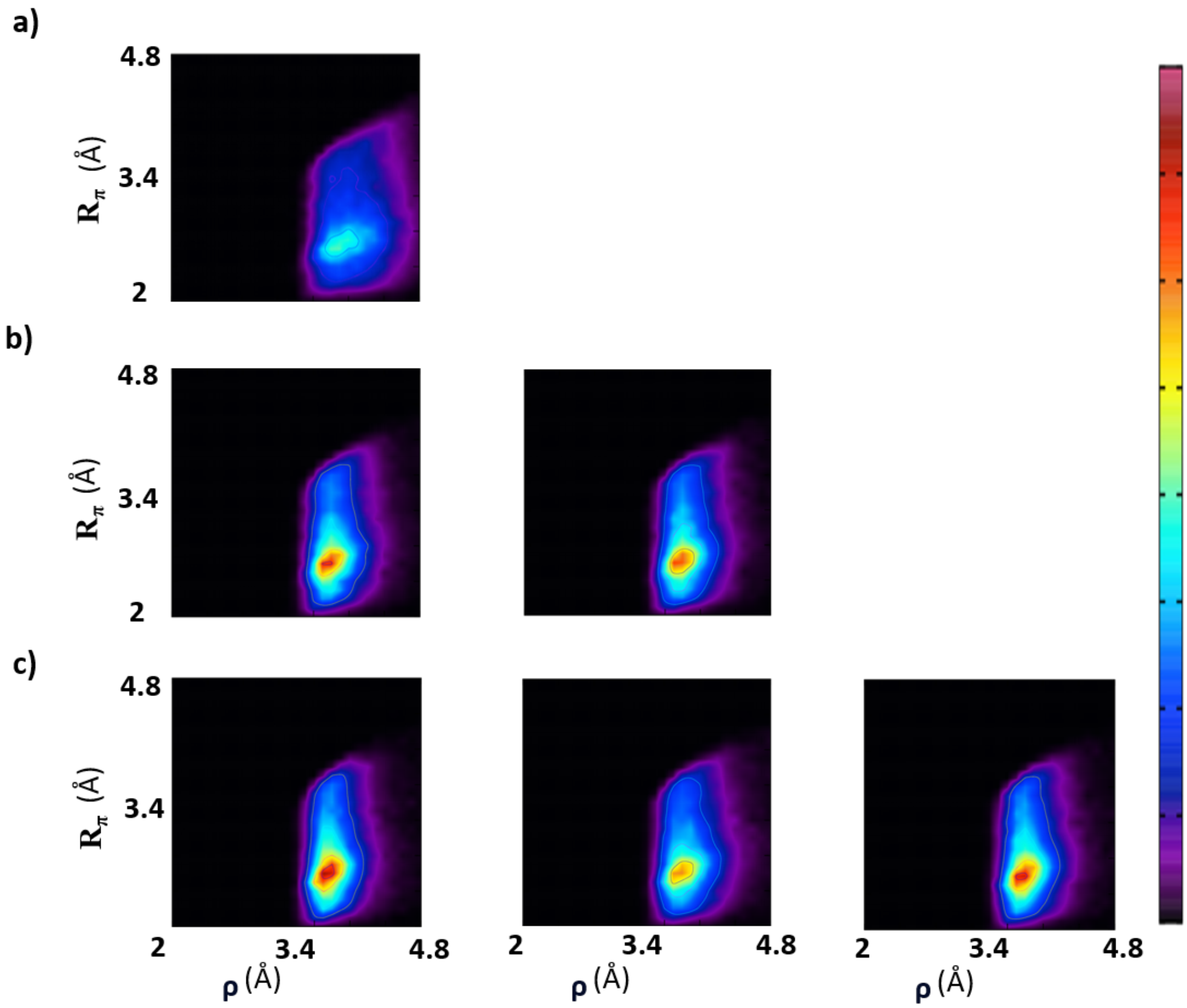

Figure S12: 2D heat maps of the distributions of the ρ and R_π distances (Å), computed along 1 μs trajectory produced for a) **PDI$_2$**@H_2O, b) **PDI$_3$**@H_2O, c) **PDI$_4$**@H_2O. In each panel, columns refer to a different *k*-*l* pair within the considered aggregate, i.e., from left to right, to the a-b, b-c and c-d units.

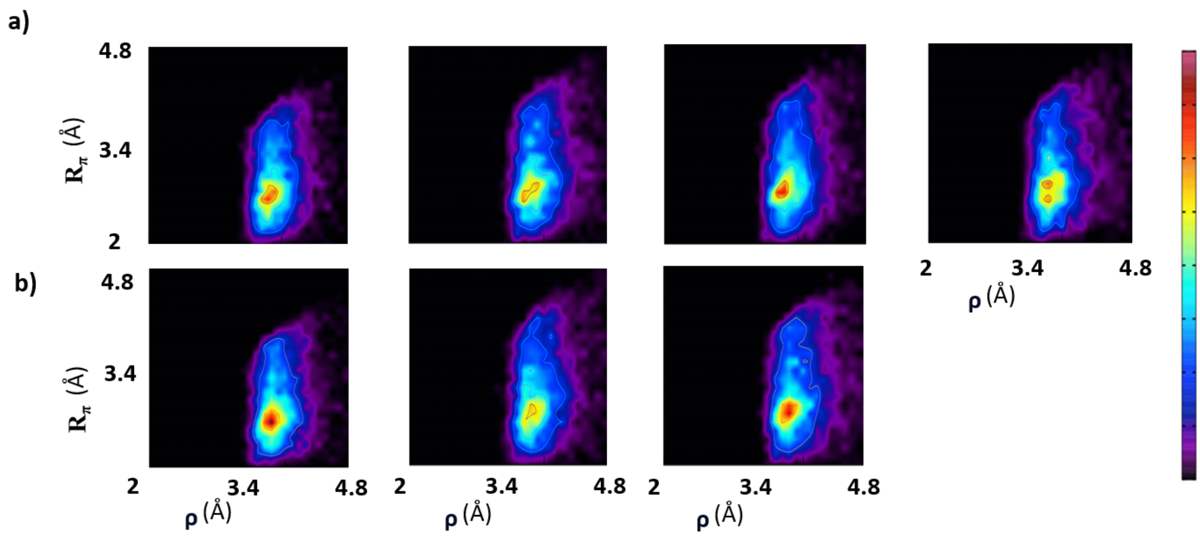

Figure S13: 2D heat maps of the distributions of the ρ and R_π distances (Å), computed along 500 ns trajectory produced for $\mathbf{PDI_8}@H_2O$. A separate plot is displayed in sequential order for each considered unit pair *k*-*l* within the octamer, from a-b (top left) to h-i (bottom right).

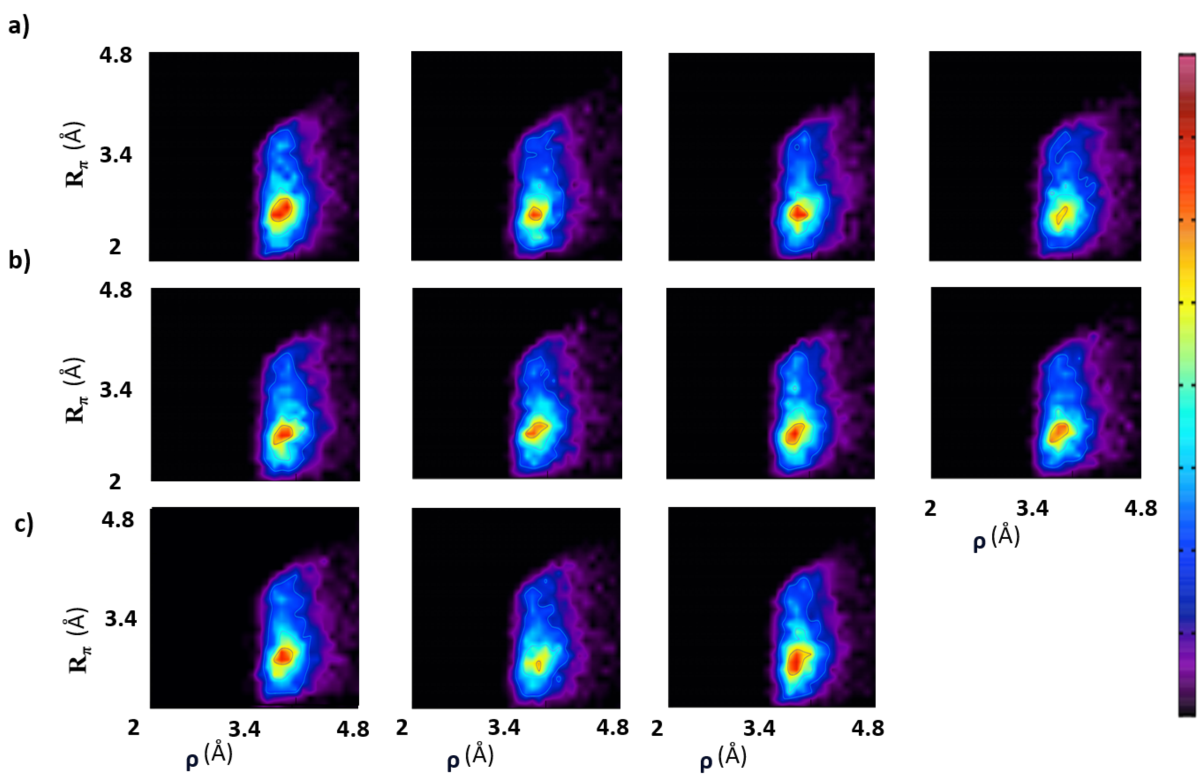

Figure S14: 2D heat maps of the distributions of the ρ and R_π distances (Å), computed along 500 ns trajectory produced for $\mathbf{PDI_{12}}@H_2O$. A separate plot is displayed in sequential order for each considered unit pair *k*-*l* within the dodecamer, from a-b (top left) to l-m (bottom right).

Sliding

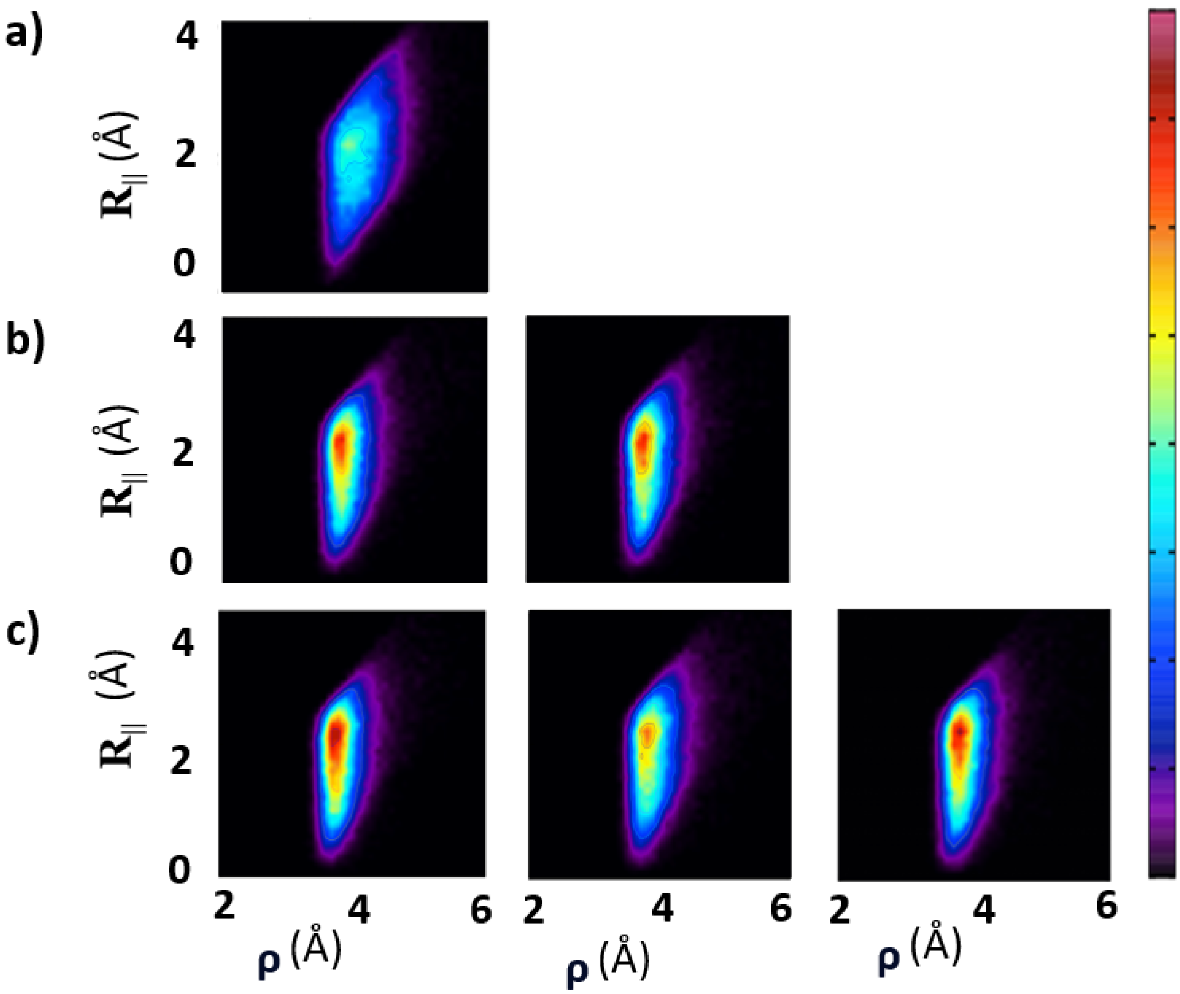

Figure S15: 2D heat maps of the distributions of the ρ and $R_{\|}$ distances (Å), computed along 1 μs trajectory produced for a) $\mathbf{PDI_2}@H_2O$, b) $\mathbf{PDI_3}@H_2O$, c) $\mathbf{PDI_4}@H_2O$. In each panel, columns refer to a different *k*-*l* pair within the considered aggregate, i.e., from left to right, to the a-b, b-c and c-d units.

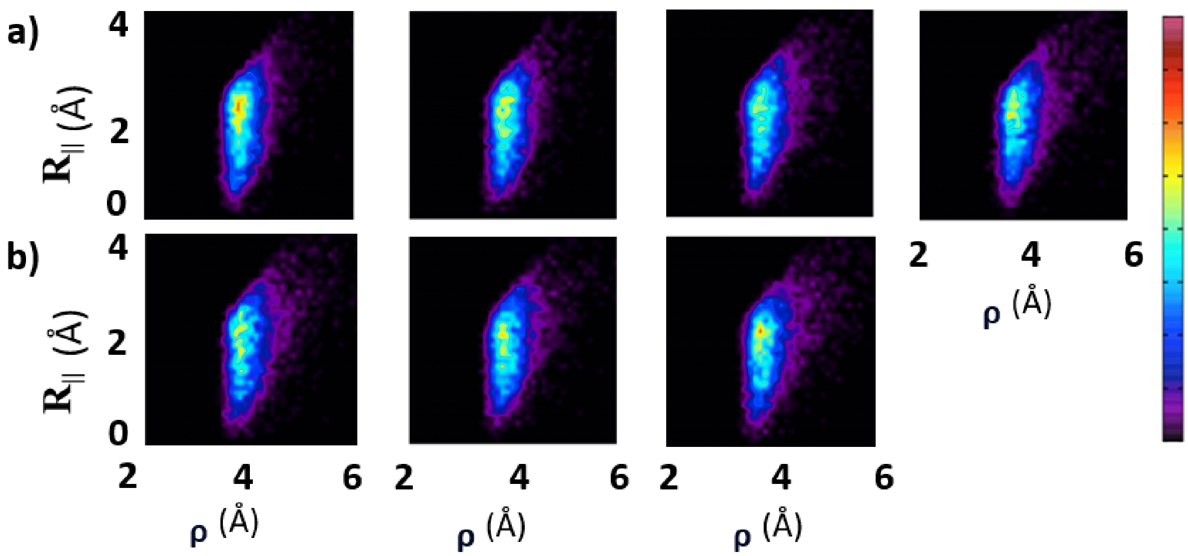

Figure S16: 2D heat maps of the distributions of the ρ and $R_{\parallel}$ distances (Å), computed along 500 ns trajectory produced for $\mathbf{PDI_8}@H_2O$. A separate plot is displayed in sequential order for each considered unit pair *k*-*l* within the octamer, from a-b (top left) to h-i (bottom right).

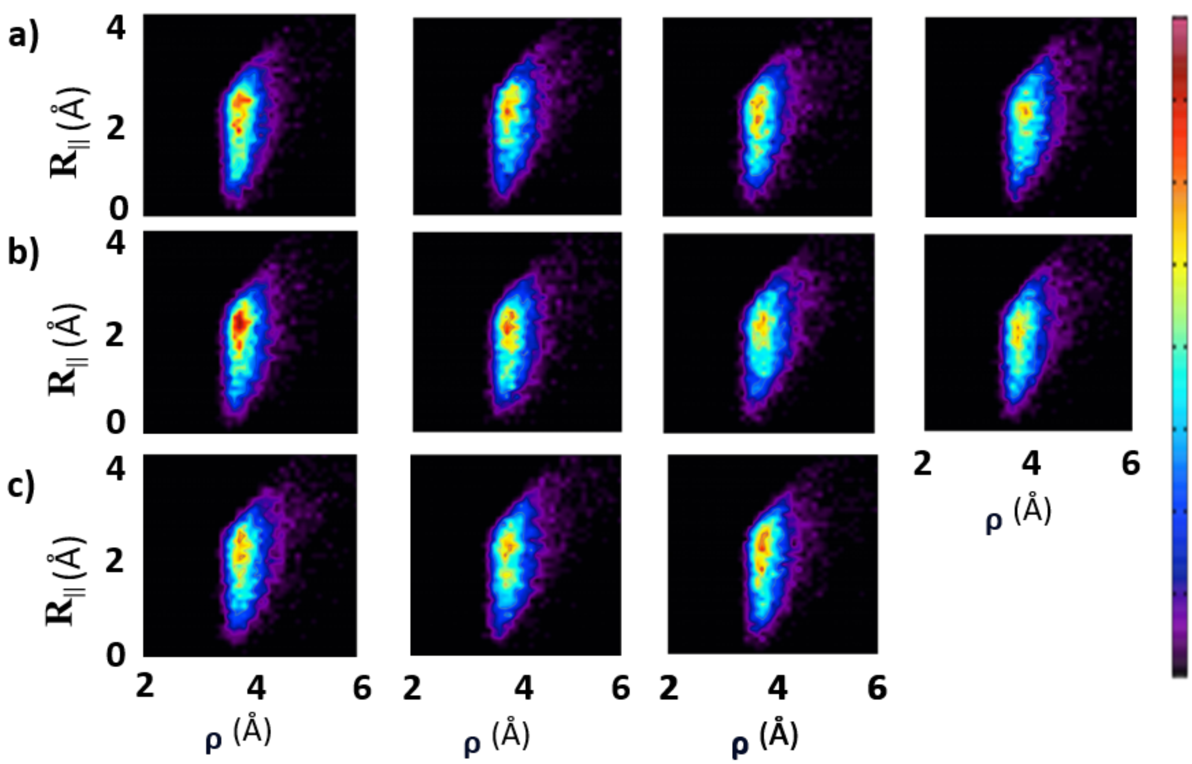

Figure S17: 2D heat maps of the distributions of the ρ and $R_{\parallel}$ distances (Å), computed along 500 ns trajectory produced for $\mathbf{PDI_{12}}@H_2O$. A separate plot is displayed in sequential order for each considered unit pair *k*-*l* within the dodecamer, from a-b (top left) to l-m (bottom right).

Shifting

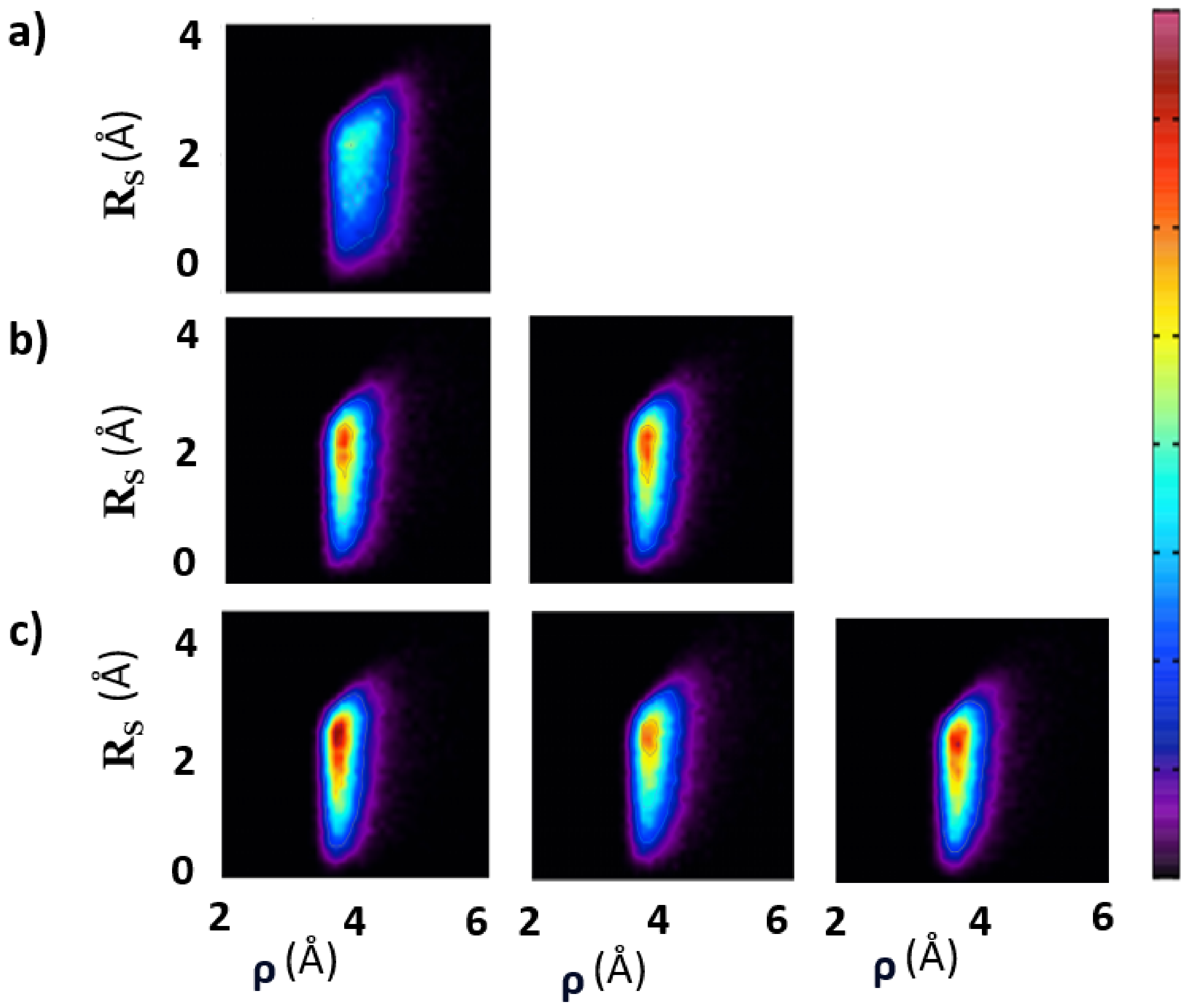

Figure S18: 2D heat maps of the distributions of the ρ and R_S distances (Å), computed along 1 μs trajectory produced for a) **PDI$_2$**@H_2O, b) **PDI$_3$**@H_2O, c) **PDI$_4$**@H_2O. In each panel, columns refer to a different *k*-*l* pair within the considered aggregate, i.e., from left to right, to the a-b, b-c and c-d units.

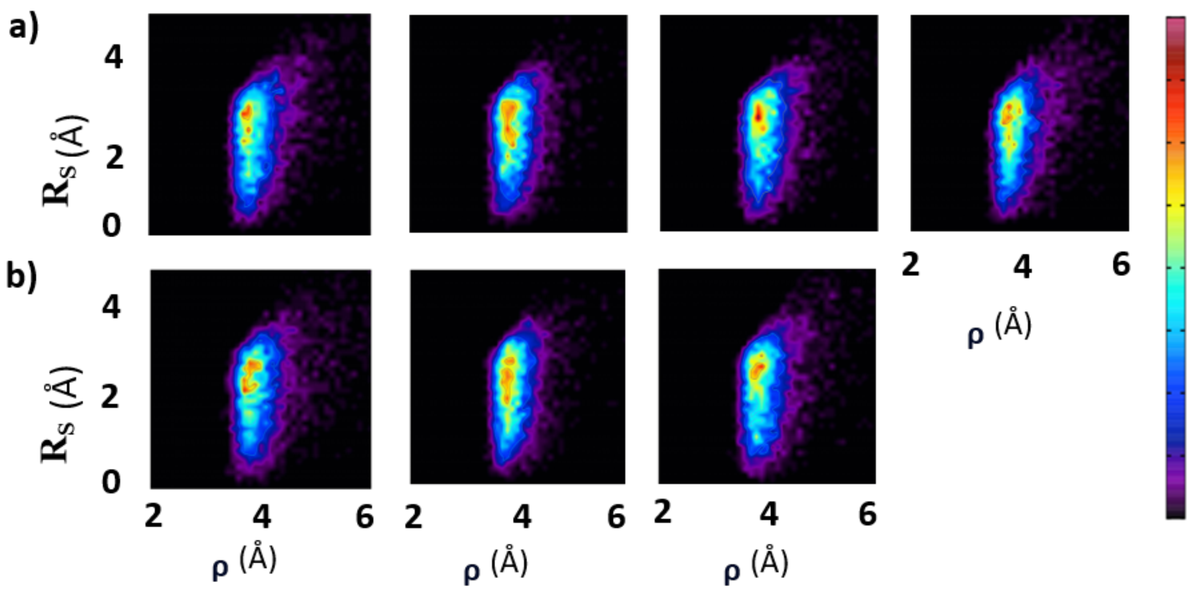

Figure S19: 2D heat maps of the distributions of the ρ and R_S distances (Å), computed along 500 ns trajectory produced for $\mathbf{PDI_8}@H_2O$. A separate plot is displayed in sequential order for each considered unit pair *k*-*l* within the octamer, from a-b (top left) to h-i (bottom right).

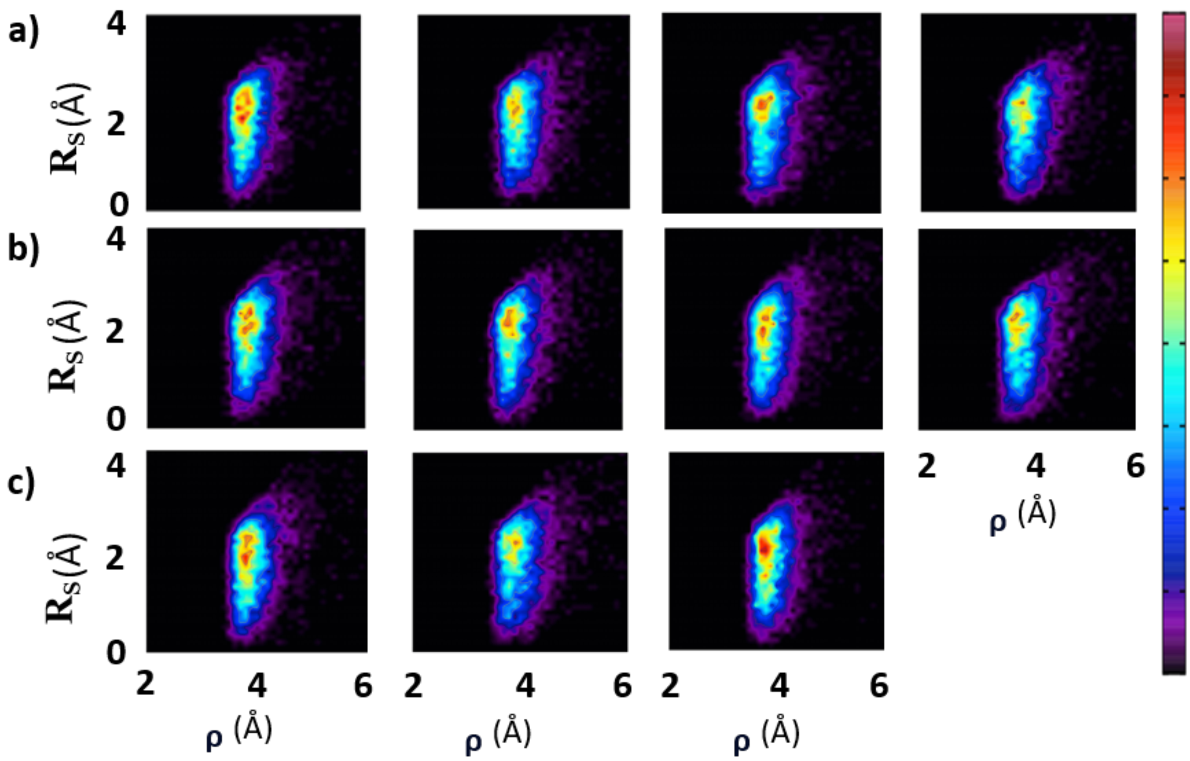

Figure S20: 2D heat maps of the distributions of the ρ and R_S distances (Å), computed along 500 ns trajectory produced for **PDI₁₂**@H_2O. A separate plot is displayed in sequential order for each considered unit pair *k*-*l* within the dodecamer, from a-b (top left) to l-m (bottom right).

B.3.2 Rotational dynamics

Spinning

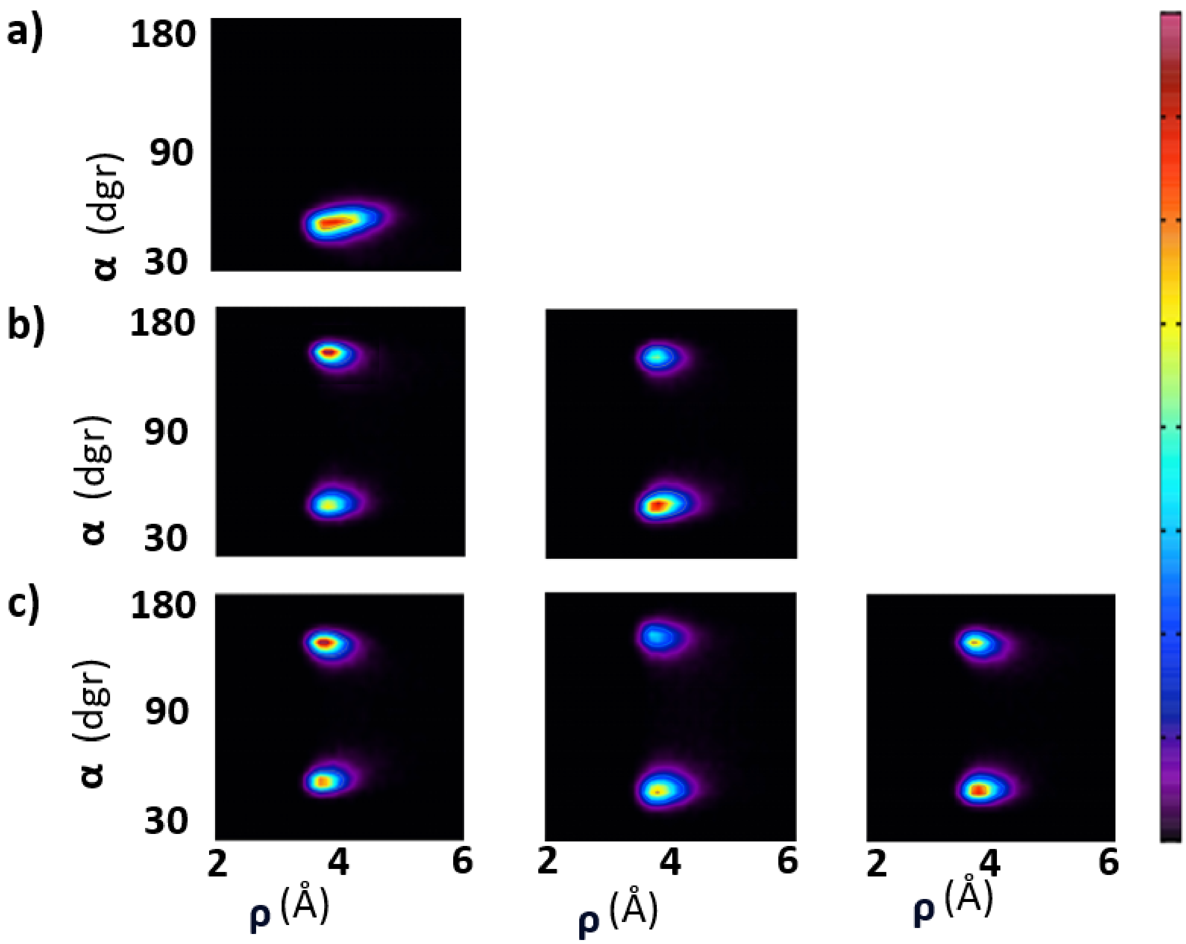

Figure S21: 2D heat maps of the distributions of the ρ distance (Å) and the α spinning angle (degr), computed along 1 μs trajectory produced for a) **PDI$_2$**@H_2O, b) **PDI$_3$**@H_2O, c) **PDI$_4$**@H_2O. In each panel, columns refer to a different *k*-*l* pair within the considered aggregate, i.e., from left to right, to the a-b, b-c and c-d units.

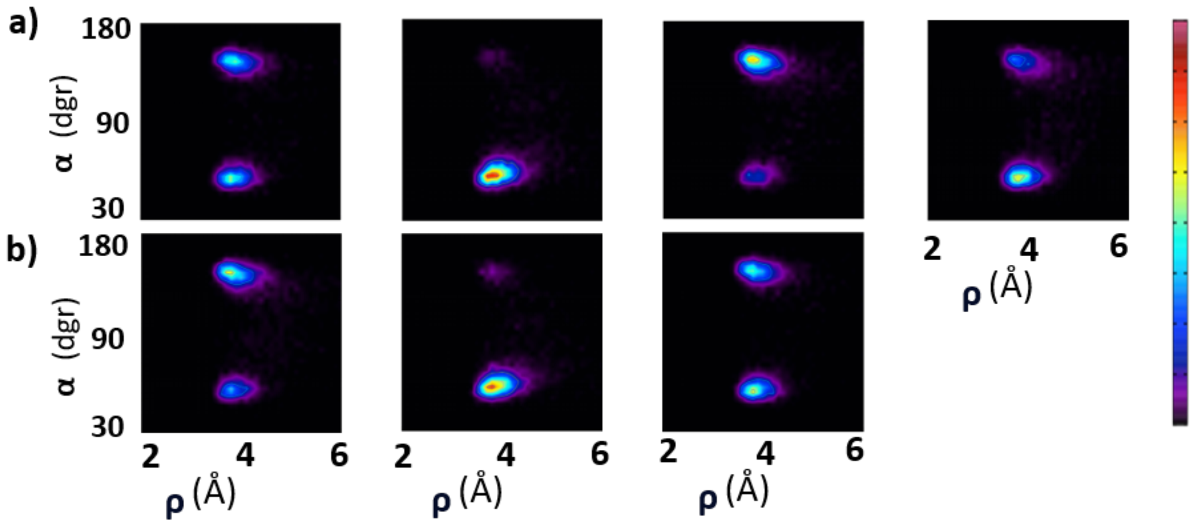

Figure S22: 2D heat maps of the distributions of the the ρ distance (Å) and the α spinning angle (degr), computed along 500 ns trajectory produced for $\mathbf{PDI_8}$@H_2O. A separate plot is displayed in sequential order for each considered unit pair *k*-*l* within the octamer, from a-b (top left) to h-i (bottom right).

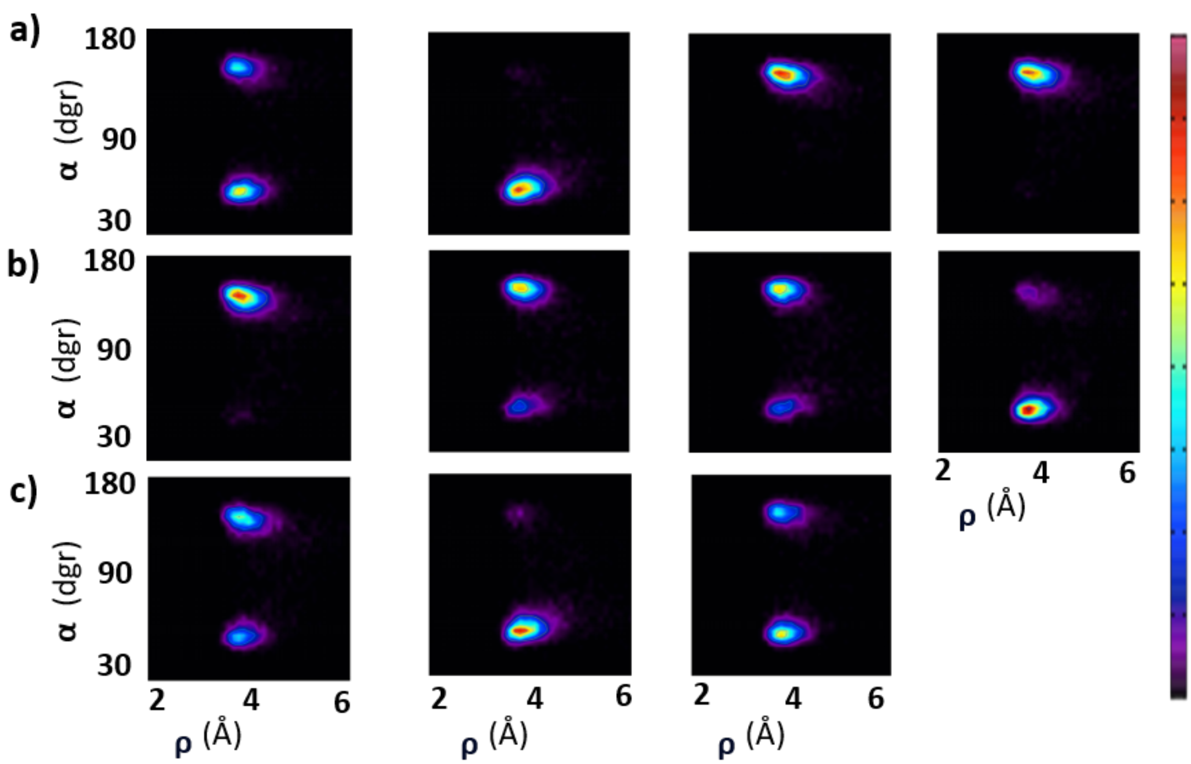

Figure S23: 2D heat maps of the distributions of the ρ distance (Å) and the α spinning angle (degr), computed along 500 ns trajectory produced for $\mathbf{PDI_{12}}$@H_2O. A separate plot is displayed in sequential order for each considered unit pair *k*-*l* within the dodecamer, from a-b (top left) to l-m (bottom right).

Rolling

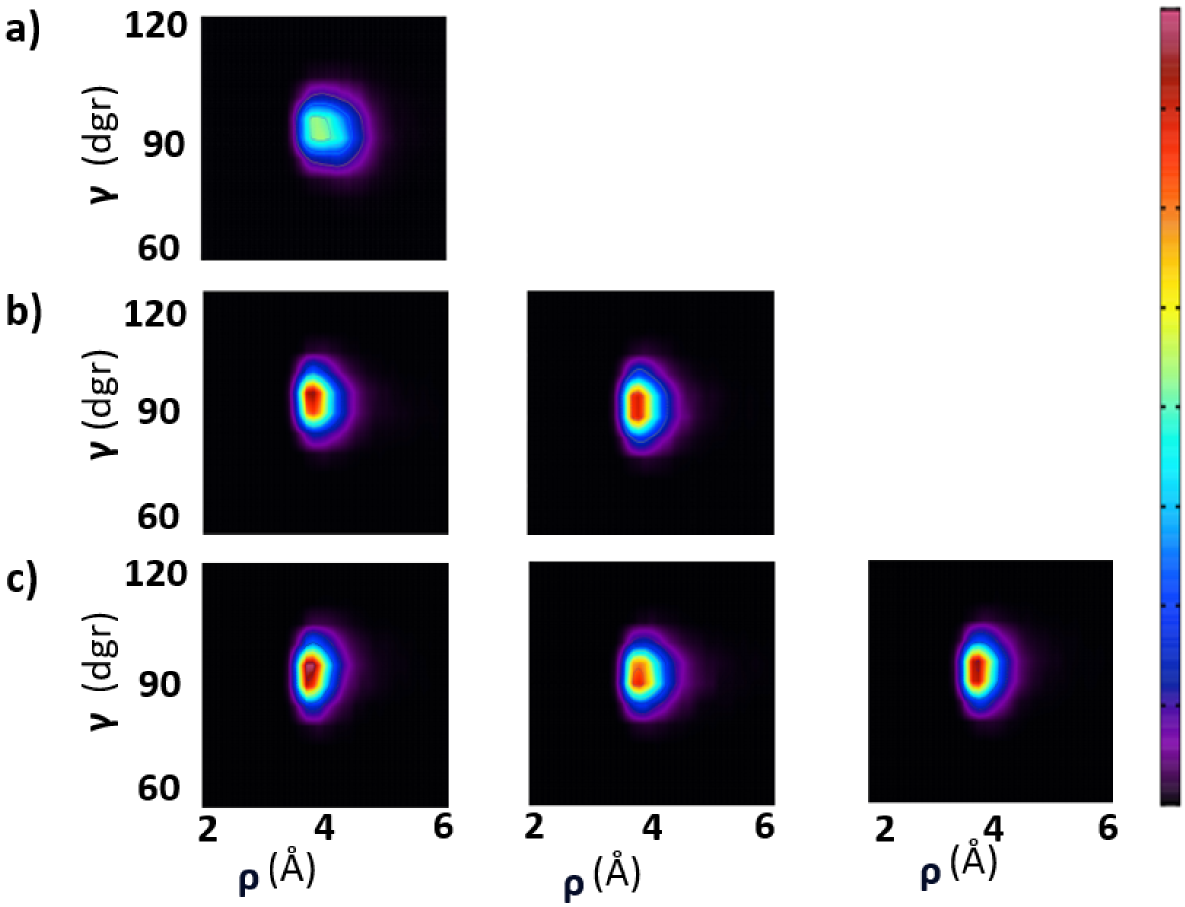

Figure S24: 2D heat maps of the distributions of the ρ distance (Å) and the γ rolling angle (degr), computed along 1 μs trajectory produced for a) **PDI$_2$**@H_2O, b) **PDI$_3$**@H_2O, c) **PDI$_4$**@H_2O. In each panel, columns refer to a different *k*-*l* pair within the considered aggregate, i.e., from left to right, to the a-b, b-c and c-d units.

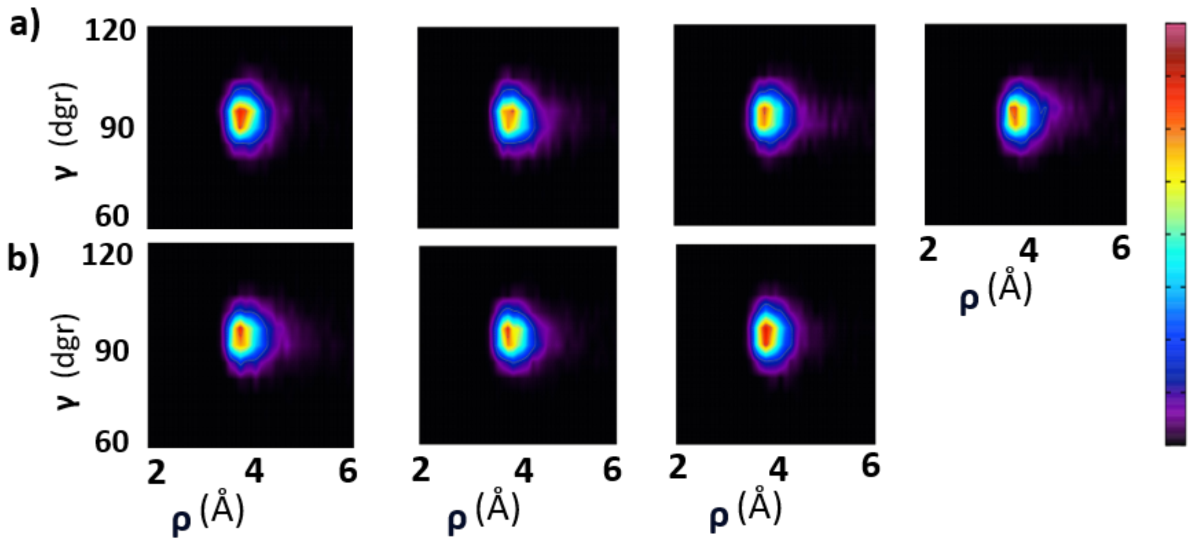

Figure S25: 2D heat maps of the distributions of the the ρ distance (Å) and the γ rolling angle (degr), computed along 500 ns trajectory produced for $\mathbf{PDI_8}@H_2O$. A separate plot is displayed in sequential order for each considered unit pair *k*-*l* within the octamer, from a-b (top left) to h-i (bottom right).

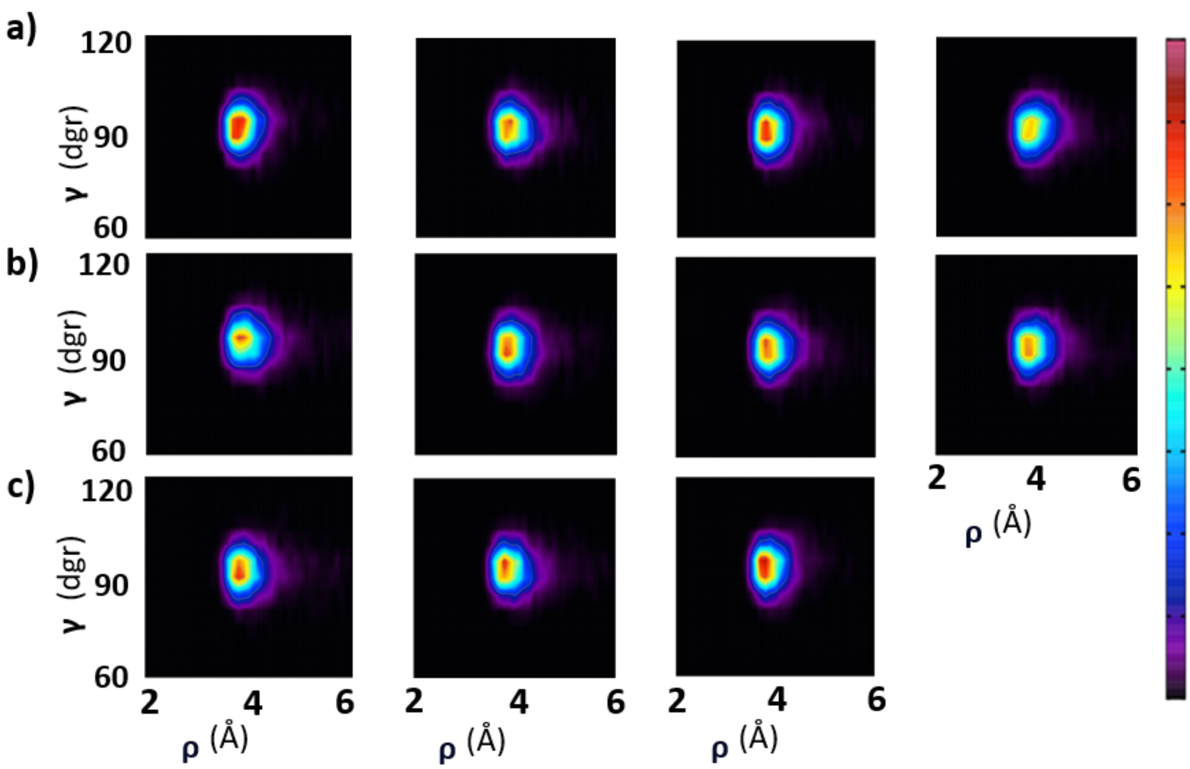

Figure S26: 2D heat maps of the distributions of the ρ distance (Å) and the γ rolling angle (degr), computed along 500 ns trajectory produced for **PDI$_{12}$**@H_2O. A separate plot is displayed in sequential order for each considered unit pair *k*-*l* within the dodecamer, from a-b (top left) to l-m (bottom right).

Tumbling

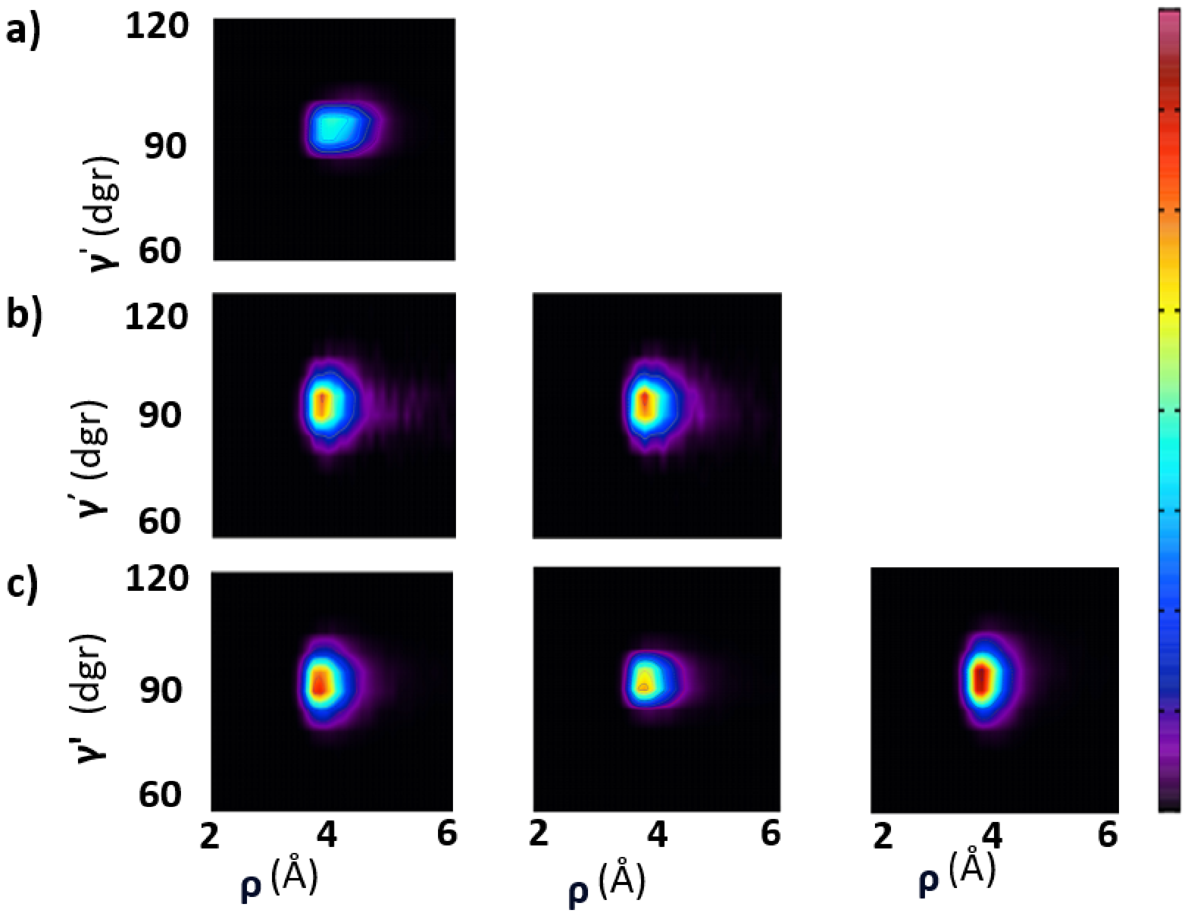

Figure S27: 2D heat maps of the distributions of the ρ distance (Å) and the γ' tumbling angle (degr), computed along 1 μs trajectory produced for a) $\mathbf{PDI_2}$@H_2O, b) $\mathbf{PDI_3}$@H_2O, c) $\mathbf{PDI_4}$@H_2O. In each panel, columns refer to a different *k*-*l* pair within the considered aggregate, i.e., from left to right, to the a-b, b-c and c-d units.

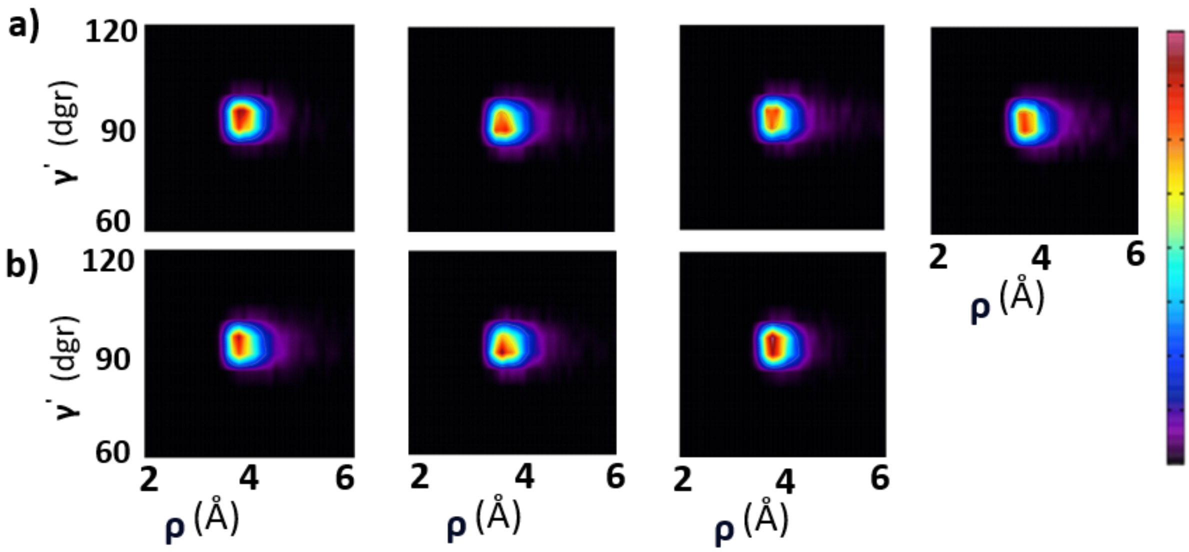

Figure S28: 2D heat maps of the distributions of the the ρ distance (Å) and the γ' tumbling angle (degr), computed along 500 ns trajectory produced for $\mathbf{PDI_8}@H_2O$. A separate plot is displayed in sequential order for each considered unit pair *k*-*l* within the octamer, from a-b (top left) to h-i (bottom right).

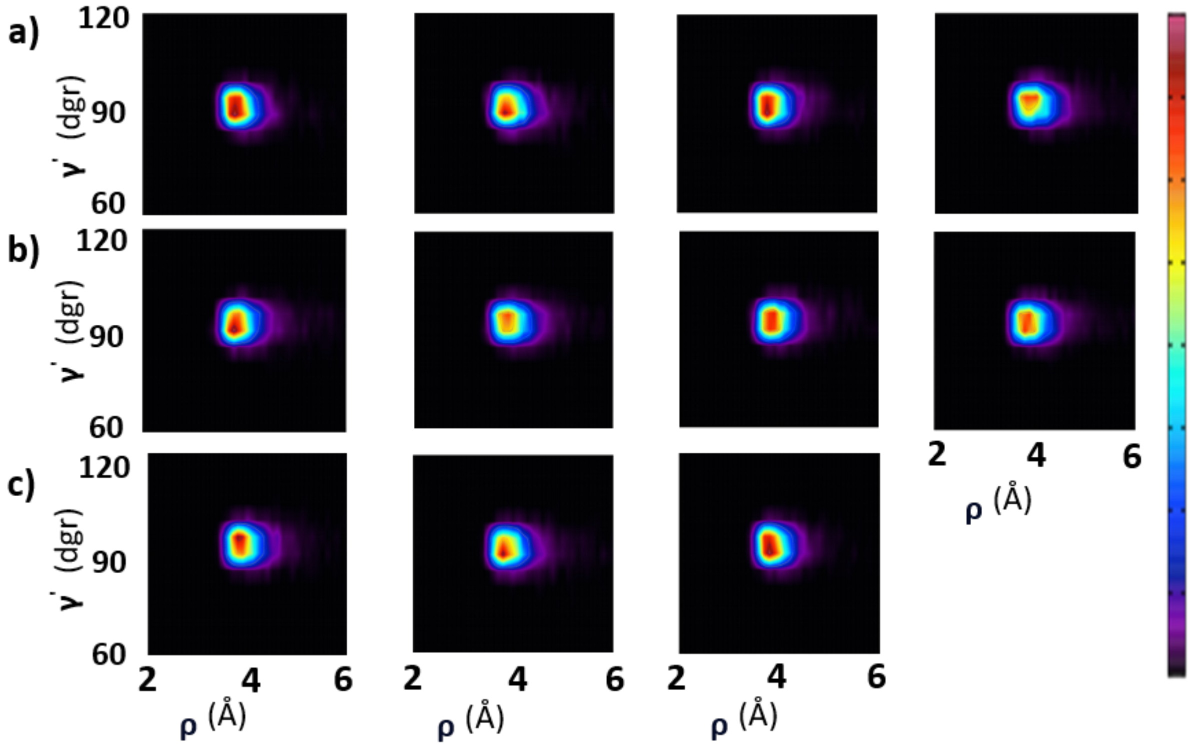

Figure S29: 2D heat maps of the distributions of the ρ distance (Å) and the γ' tumbling angle (degr), computed along 500 ns trajectory produced for $\mathbf{PDI_{12}}@H_2O$. A separate plot is displayed in sequential order for each considered unit pair *k*-*l* within the dodecamer, from a-b (top left) to l-m (bottom right).

B.3.3 Columnar dephasing

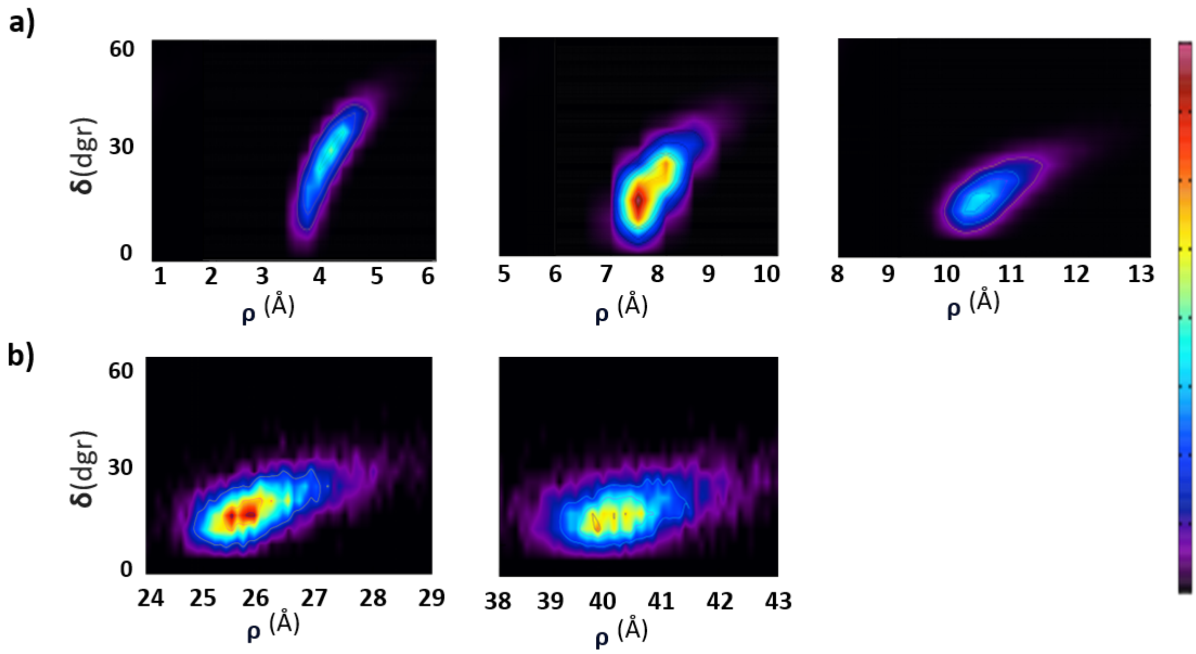

Figure S30: 2D heat maps of the distributions of the ρ distance (Å) between the first and last unit of the considered aggregate and the δ dephasing angle (degr) of the last unit of each aggregate, computed along the trajectory produced for: a) $\mathbf{PDI_2}@H_2O$, $\mathbf{PDI_3}@H_2O$ and $\mathbf{PDI_4}@H_2O$; b) $\mathbf{PDI_8}@H_2O$ and $\mathbf{PDI_{12}}@H_2O$.

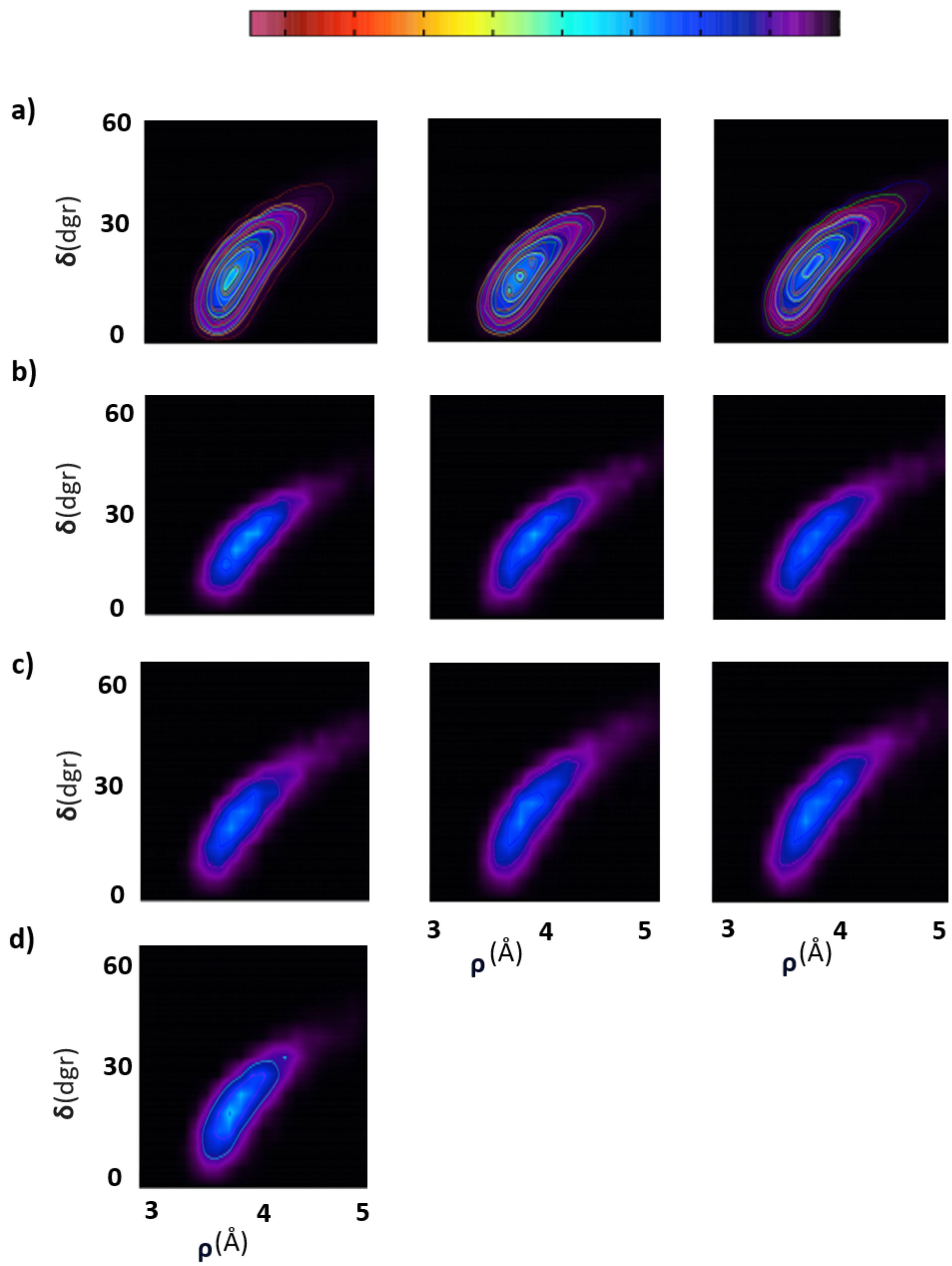

Figure S31: 2D heat maps of the distributions ρ (Å) and δ dephasing angle (degr), computed along 1 μs trajectory produced for $\mathbf{PDI_4}@H_2O$ and along 500 ns trajectory produced for $\mathbf{PDI_8}@H_2O$. A separate plot is displayed in sequential order for each considered unit pair *k-l* within: a) the tetramer and b)-d) octamer from a-b to l-m pairs.

C Solute-solvent radial distribution functions

C.1 Solute reference atoms

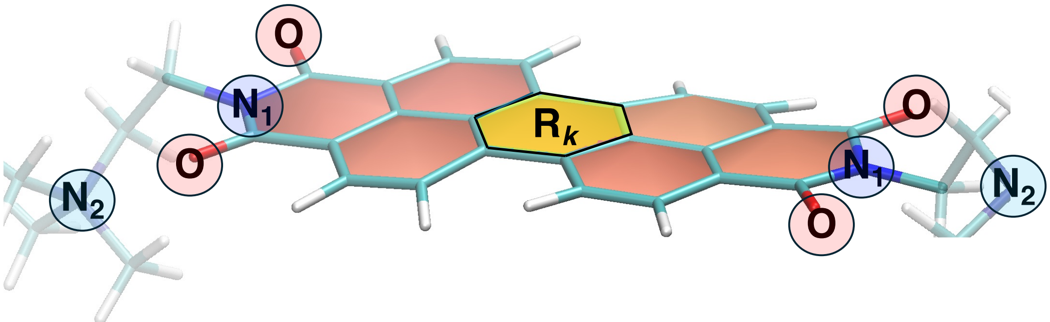

Figure S32: Labels of the reference sites α, considered for each stacked k unit for the calculation of the $g_{\alpha-H_w}$(r) and $g_{\alpha-O_w}$(r) radial distribution functions, where H_w and O_w are the water proton and oxygen, while α=N_1, N_2, O or R_k.

C.2 $\mathbf{PDI}_2@H_2O$

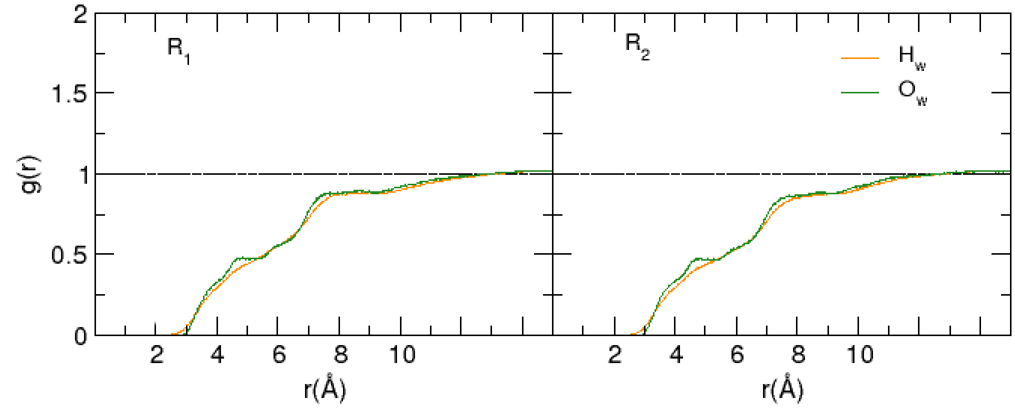

Figure S33: Pair-correlation functions $g_{R_k-H_w}$ (orange) and $g_{R_k-O_w}$ (green), computed along the $\mathbf{PDI_2}@H_2O$ trajectory, between the central ring (R_k, see Fig S32) of each stacked PDI unit k and the water proton or oxygen, respectively.

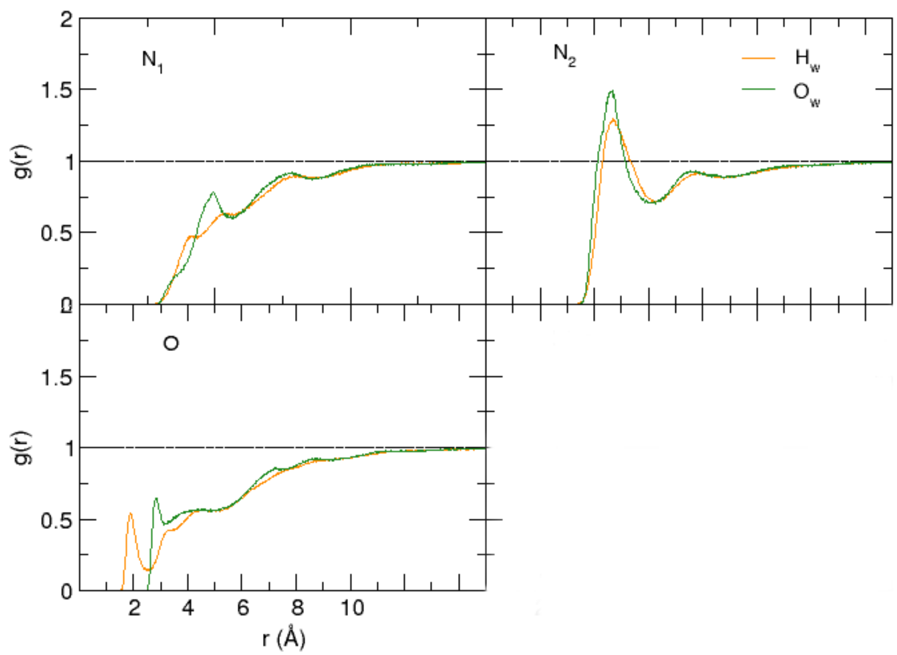

Figure S34: Pair-correlation functions $g_{\alpha-H_w}$ (orange) and $g_{\alpha-O_w}$ (green), computed along the $\mathbf{PDI_2}@H_2O$ trajectory, between the α site (α= N_1, $N2$, O, see Fig S32) of PDI monomer a (see Fig S1) and the water proton or oxygen, respectively. Negligible differences were found with the same radial distribution functions computed for monomer b (see Fig S1).

C.3 PDI$_3$@H_2O

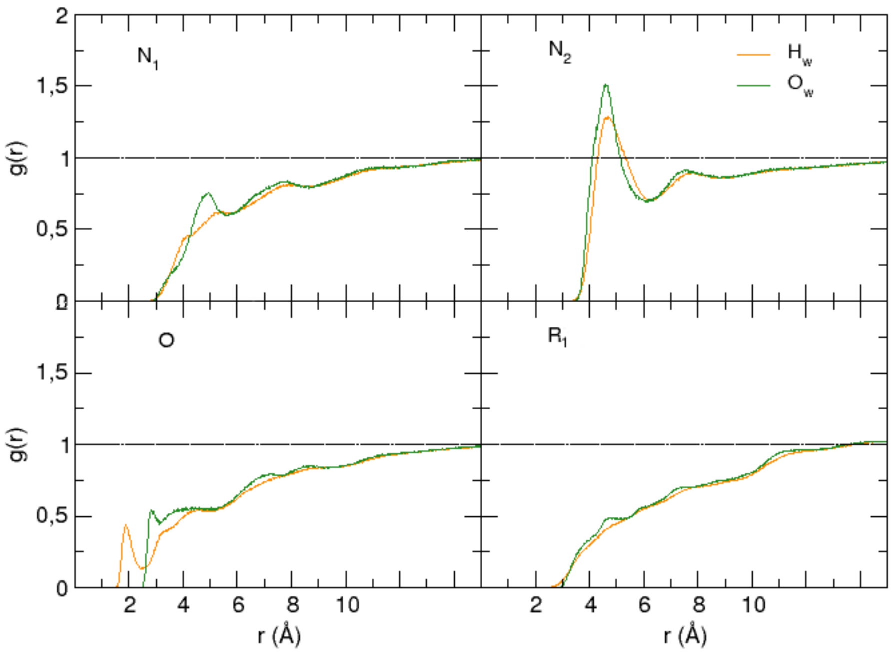

Figure S35: Pair-correlation functions $g_{\alpha-H_w}$ (orange) and $g_{\alpha-O_w}$ (green), computed along the **PDI$_3$**@H_2O trajectory, between the α site (α= N_1, $N2$, O or R$_1$) of PDI monomer a (see Fig S1) and the water proton or oxygen, respectively. Negligible differences were found with the same radial distribution functions computed for monomer c (see Fig S1).

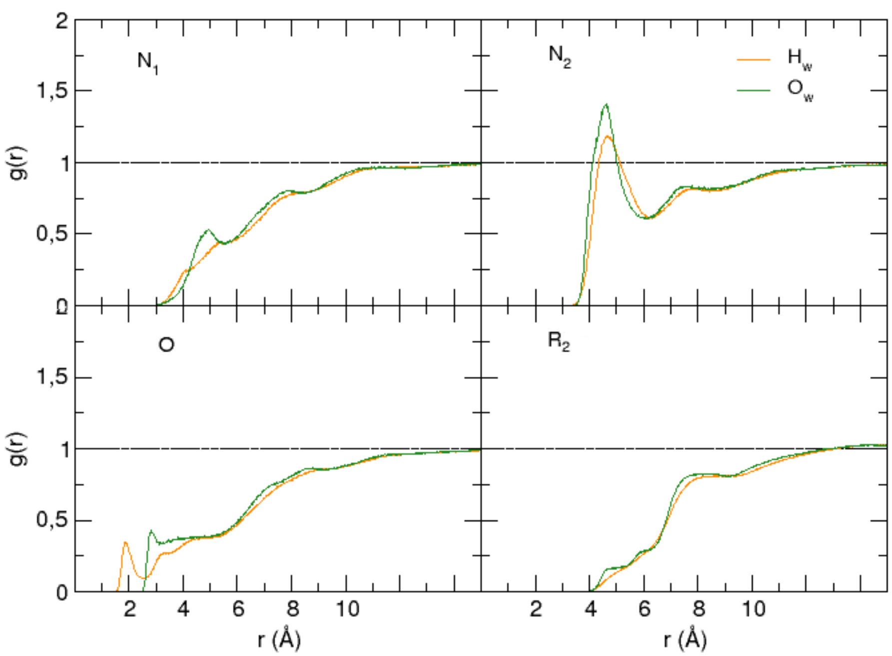

Figure S36: Pair-correlation functions $g_{\alpha-H_w}$ (orange) and $g_{\alpha-O_w}$ (green), computed along the $\mathbf{PDI_3}@H_2O$ trajectory, between the α site (α= N_1, N_2, O or R_2 of PDI monomer b (see Fig S1) and the water proton or oxygen, respectively.)

C.4 PDI$_4$@H_2O

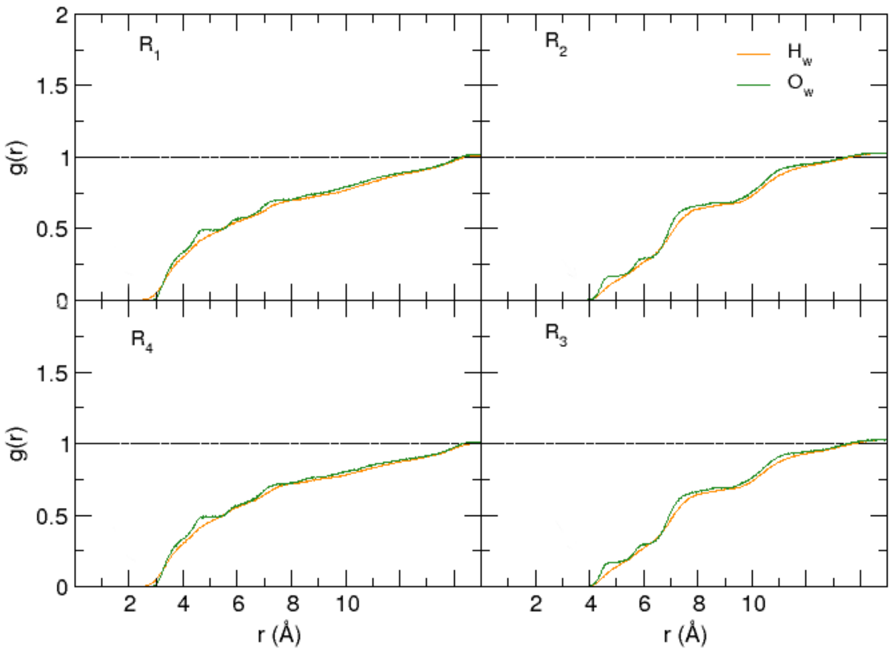

Figure S37: Pair-correlation functions $g_{R_k-H_w}$ (orange) and $g_{R_k-O_w}$ (green), computed along the **PDI$_4$**@H_2O trajectory, between the central ring (R$_k$, see Fig S32) of each stacked PDI unit k and the water proton or oxygen, respectively.

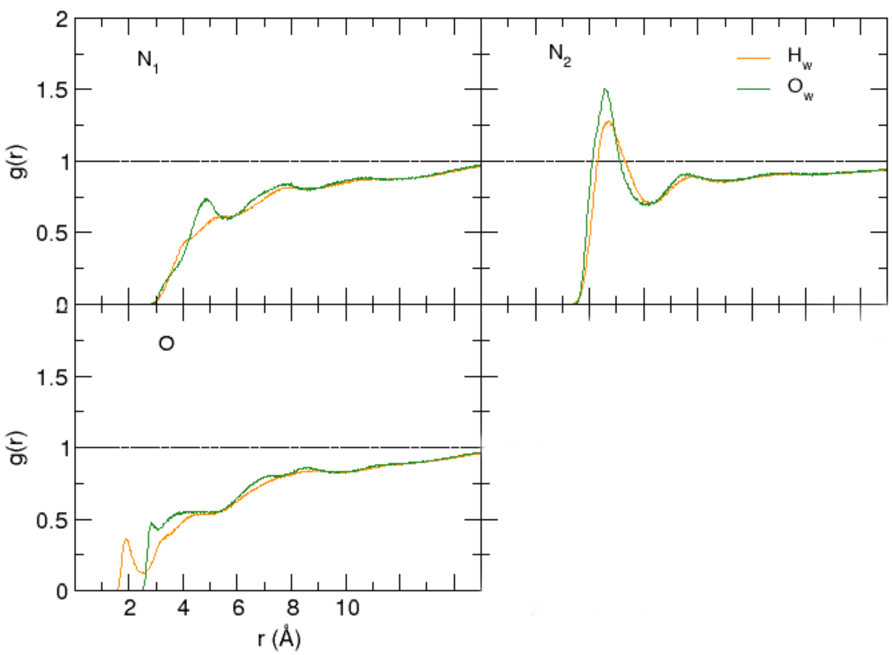

Figure S38: Pair-correlation functions $g_{\alpha-H_w}$ (orange) and $g_{\alpha-O_w}$ (green), computed along the **PDI_4**@H_2O trajectory, between the α site (α= N_1, $N2$, O, see Fig S32) of the external PDI monomer a (see Fig S1) and the water proton or oxygen, respectively. Negligible differences were found with the same radial distribution functions computed for the other external monomer d (see Fig S1).

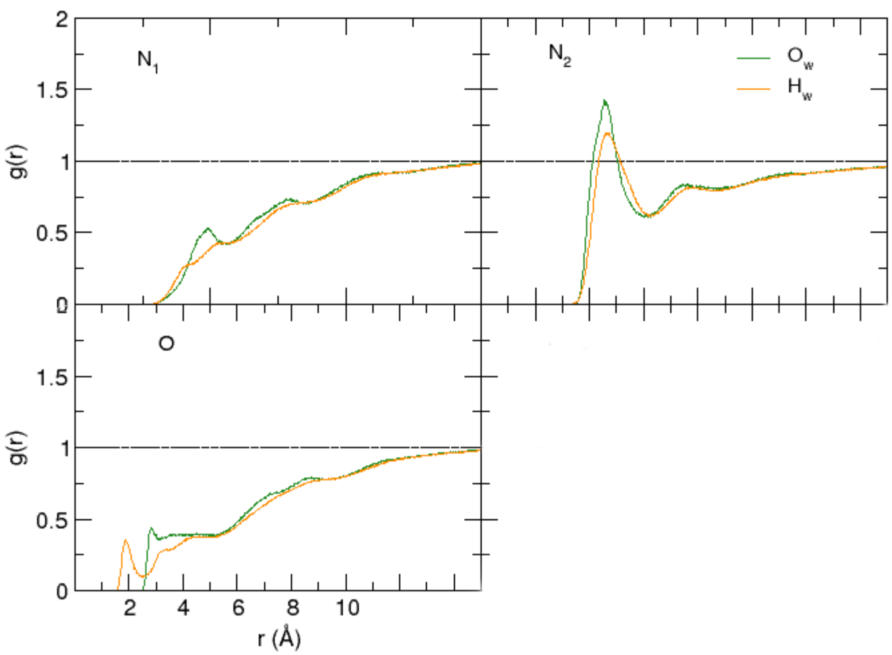

Figure S39: Pair-correlation functions $g_{\alpha-H_w}$ (orange) and $g_{\alpha-O_w}$ (green), computed along the **PDI4**@H_2O trajectory, between the α site (α= N_1, $N2$, O, see Fig S32) of the inner PDI monomer b (see Fig S1) and the water proton or oxygen, respectively. Negligible differences were found with the same radial distribution functions computed for the other inner monomer c (see Fig S1).

C.5 $PDI_8@H_2O$

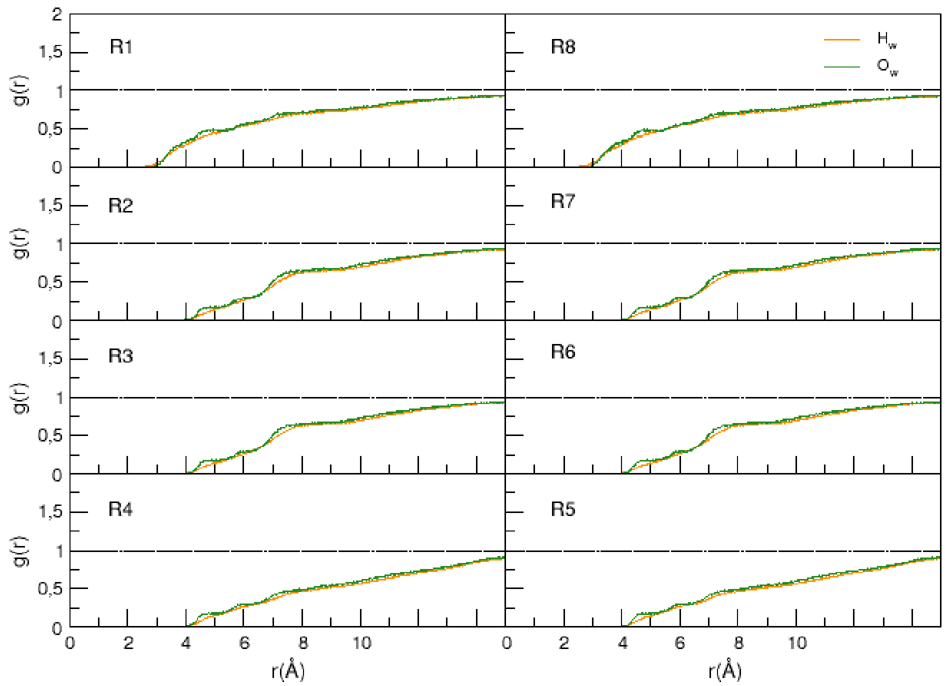

Figure S40: Pair-correlation functions $g_{R_k-H_w}$ (orange) and $g_{R_k-O_w}$ (green), computed along the $\mathbf{PDI_8}@H_2O$ trajectory, between the central ring (R_k, see Fig S32) of each stacked PDI unit k and the water proton or oxygen, respectively.

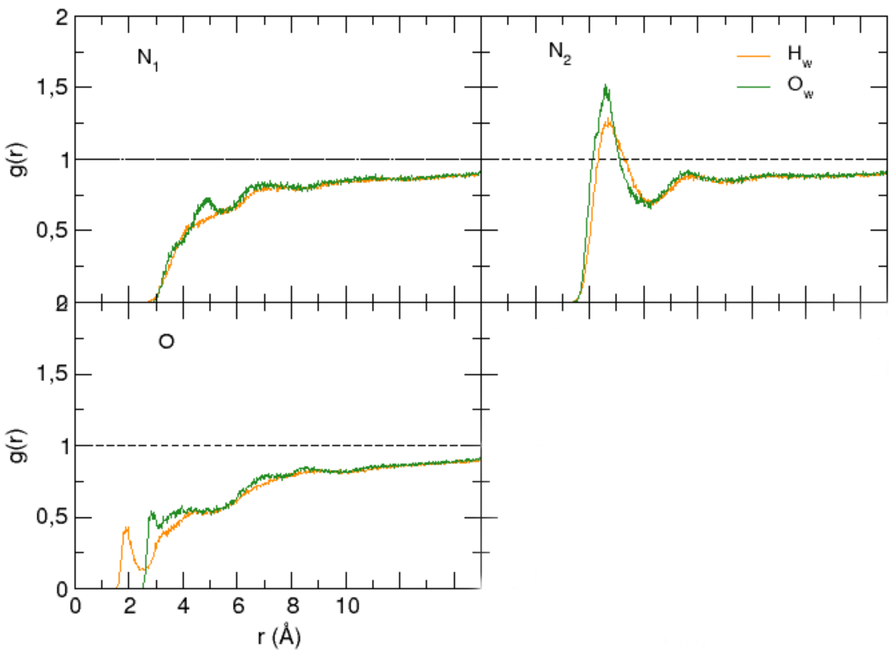

Figure S41: Pair-correlation functions $g_{\alpha-H_w}$ (orange) and $g_{\alpha-O_w}$ (green), computed along the **PDI₈**@H_2O trajectory, between the α site (α= N_1, $N2$, O, see Fig S32) of the external PDI monomer a (see Fig S1) and the water proton or oxygen, respectively. Negligible differences were found with the same radial distribution functions computed for the other external monomer h (see Fig S1).

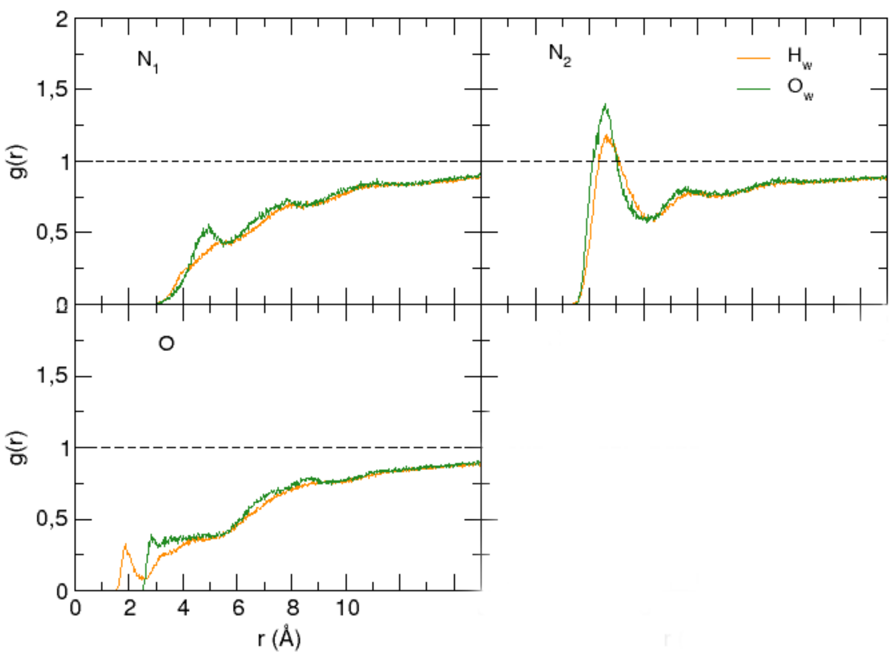

Figure S42: Pair-correlation functions $g_{\alpha-H_w}$ (orange) and $g_{\alpha-O_w}$ (green), computed along the $\mathbf{PDI_8}@H_2O$ trajectory, between the α site (α= N_1, $N2$, O, see Fig S32) of the PDI monomer b (see Fig S1) and the water proton or oxygen, respectively. Negligible differences were found with the same radial distribution functions computed for the other symmetric monomer g (see Fig S1).

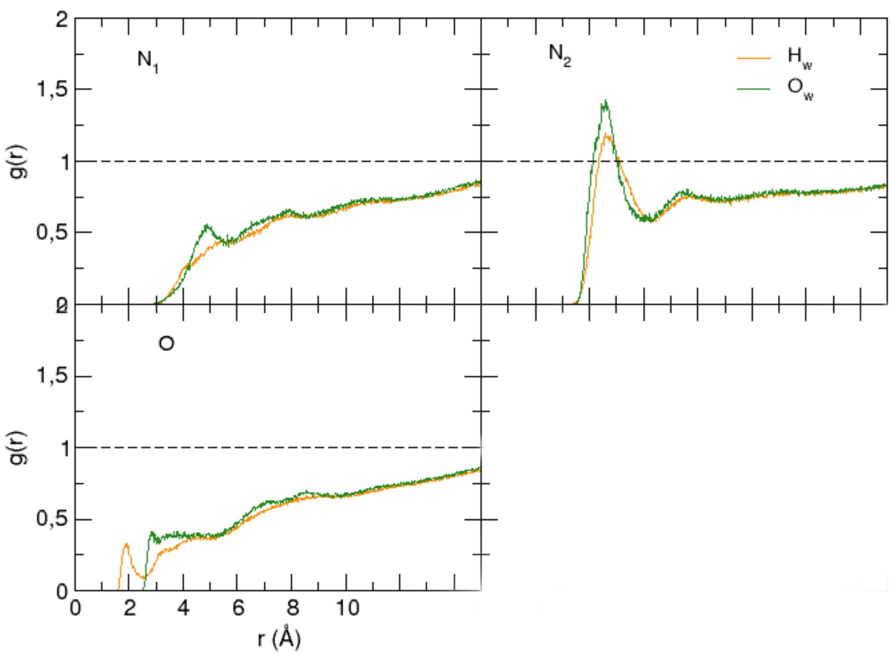

Figure S43: Pair-correlation functions $g_{\alpha-H_w}$ (orange) and $g_{\alpha-O_w}$ (green), computed along the $\mathbf{PDI_8}@H_2O$ trajectory, between the α site ($\alpha = N_1$, $N2$, O, see Fig S32) of the PDI monomer c (see Fig S1) and the water proton or oxygen, respectively. Negligible differences were found with the same radial distribution functions computed for the other symmetric monomer f (see Fig S1).

C.6 $\textbf{PDI}_{12}@H_2O$

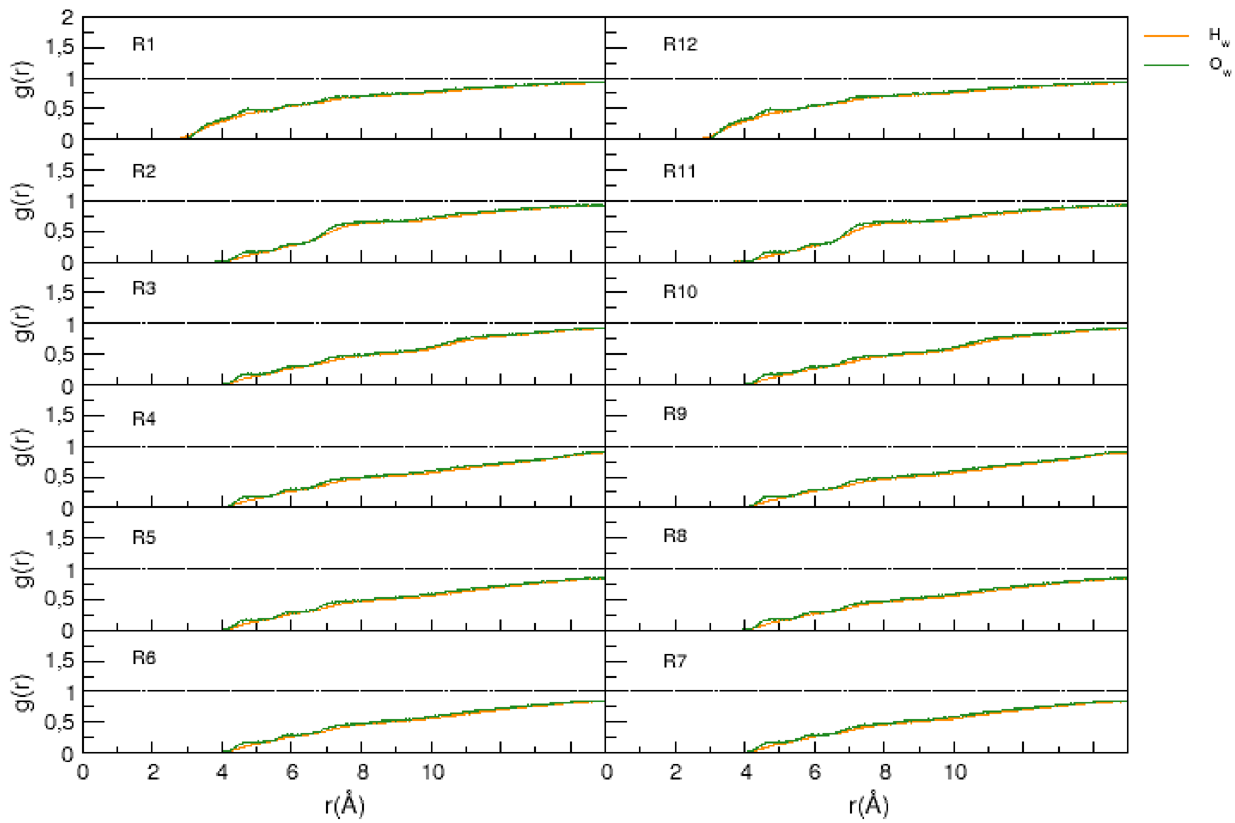

Figure S44: Pair-correlation functions $g_{R_k-H_w}$ (orange) and $g_{R_k-O_w}$ (green), computed along the $\mathbf{PDI_{12}}@H_2O$ trajectory, between the central ring (R_k, see Fig S32) of each stacked PDI unit k and the water proton or oxygen, respectively.

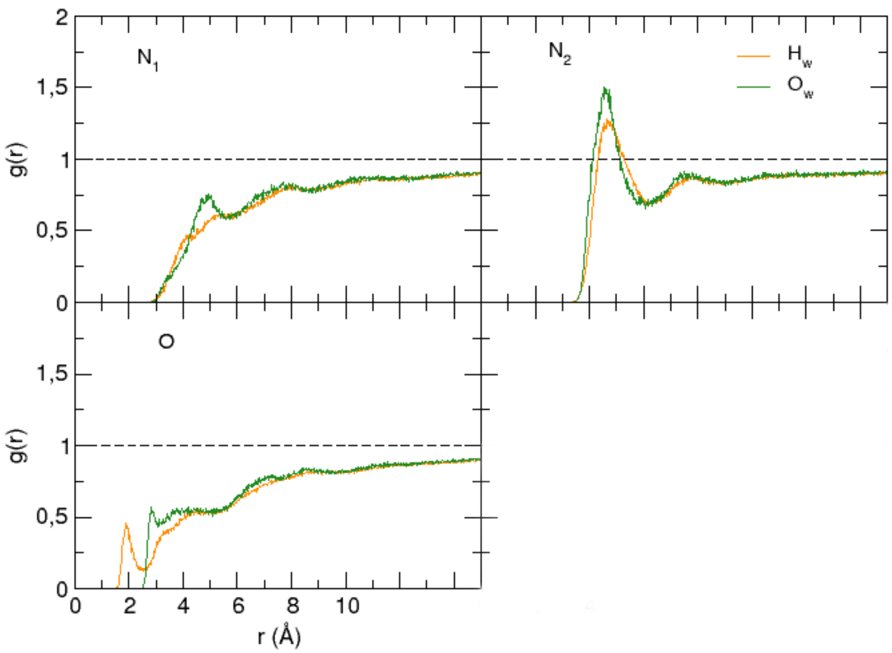

Figure S45: Pair-correlation functions $g_{\alpha-H_w}$ (orange) and $g_{\alpha-O_w}$ (green), computed along the **PDI₁₂**@H_2O trajectory, between the α site (α= N_1, $N2$, O, see Fig S32) of the external PDI monomer a (see Fig S1) and the water proton or oxygen, respectively. Negligible differences were found with the same radial distribution functions computed for the other external monomer m (see Fig S1).

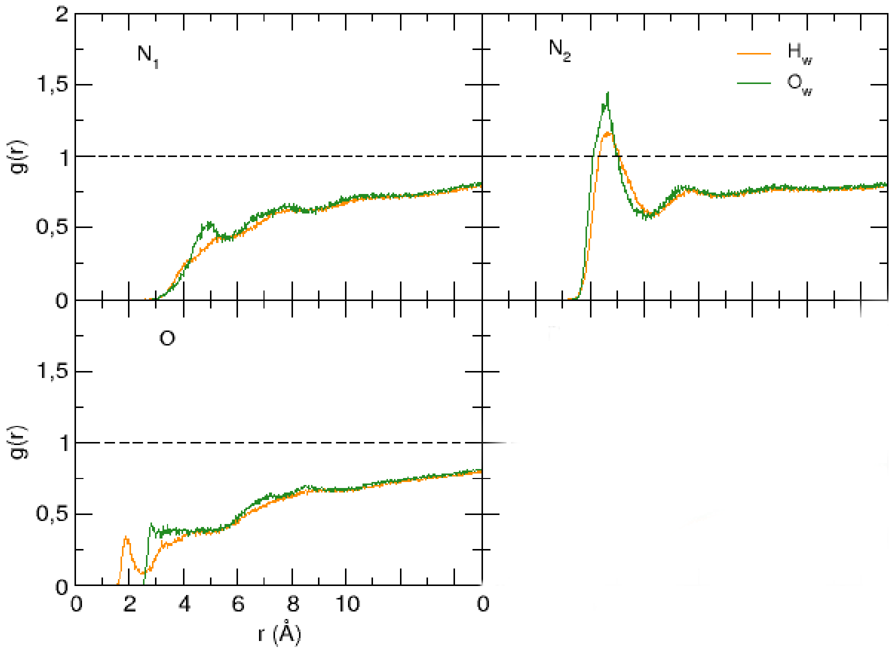

Figure S46: Pair-correlation functions $g_{\alpha-H_w}$ (orange) and $g_{\alpha-O_w}$ (green), computed along the $\mathbf{PDI_{12}}@H_2O$ trajectory, between the α site (α= N_1, $N2$, O, see Fig S32) of the inner PDI monomer f (see Fig S1) and the water proton or oxygen, respectively. Negligible differences were found with the same radial distribution functions computed for the other inner monomer g (see Fig S1).

D Aggregation Thermodynamics

D.1 Thermodynamic Analysis

The self-assembly of n PDI solvated units is driven by the binding free energy ΔG,

$$\Delta G = \Delta H_{aggr} - T\Delta S_{aggr} \tag{S1}$$

where ΔH_{aggr} and ΔS_{aggr} are the enthalpy and entropy contributions to the aggregation process. As far as the former term is concerned, ΔH_{aggr} can be defined as

$$\Delta H_{\text{aggr}} = \overline{H}_{\text{b}} - n\overline{H}_{\text{nb}} \tag{S2}$$

where $\overline{H}_{\text{b}}$ and $\overline{H}_{\text{nb}}$ are the average enthalpy of the bonded (aggregate) and non-bonded states. These can be defined along the US trajectories in terms of incremental $N \rightarrow N+1$ aggregation steps, which lead to the progressive formation of the columanr stack. These steps are defined as

$$S_{N;M} \longrightarrow S_{N+1},$$

where S_N denotes a pre-formed N-mer stack, M a single PDI monomer solvated in water and not yet aggregated, and $S_{N;M}$ the reference system containing both S_N and M in the same simulation box. For $N = 1$, $S_{1;M}$ corresponds to two independent solvated monomers, so that the step $S_{1;M} \rightarrow S_2$ describes dimerization, while for $N = 3$ and $N = 5$ the processes correspond to trimer + monomer $\rightarrow$ tetramer and pentamer + monomer $\rightarrow$ hexamer, respectively. This definition isolates the contribution of each elongation step and enables direct comparison of the enthalpic cost as the column grows. Table S5 reports ΔH_{aggr} values obtained for the dimer, tetramer and hexamer aggregates, where the positive sign registered in all cases indicates that the self-assembly is always enthalpically unfavorable, regardless the aggregates size.

Table S5: Average aggregation enthalpy $\Delta\overline{H}_{\text{aggr}}$ (kJ mol^{-1}) obtained from the MD simulations for dimer, tetramer and hexamer. $T = 300$ K, $p = 1$ bar.

$\Delta H_{\text{aggr}}(\text{PDI}_2@\text{H}_2\text{O})$	$\Delta H_{\text{aggr}}(\text{PDI}_4@\text{H}_2\text{O})$	$\Delta H_{\text{aggr}}(\text{PDI}_6@\text{H}_2\text{O})$
40 ± 32	72 ± 40	86 ± 46

Turning to the aggregation entropy ΔS_{aggr}, it can be retrieved exploiting equation (S1), from the ΔG and ΔH_{aggr} values shown in Tables S1 and S5. The final thermodynamic analysis, summarized in Table 2 of the main text for the $PDI_2@H_2O$, $PDI_4@H_2O$ and $PDI_6@H_2O$ systems, points toward a an entropically driven aggregation in all cases, the entropy gain reducing with increasing aggregate size.

D.2 Contributions to the aggregation enthalpy

To gain a deeper understanding of the enthalpic trends, we analyzed the energetics of the formation of the dimer, tetramer, and hexamer. According to thermodynamics, the enthalpy of a system can be expressed as

$$H = E^{\text{kin}} + E^{\text{pot}} + pV, \tag{S3}$$

where E^{kin} and E^{pot} are the kinetic and potential energies, and the last term is the pressure–volume contribution. Consequently, the stepwise aggregation enthalpy is written as

$$\Delta H_{\text{aggr}}^{(S_{N;M} \to S_{N+1})} = \Delta E_{\text{aggr}}^{\text{kin},(S_{N;M} \to S_{N+1})} + \Delta E_{\text{aggr}}^{\text{pot},(S_{N;M} \to S_{N+1})} + \Delta(pV)_{\text{aggr}}^{(S_{N;M} \to S_{N+1})}. \tag{S4}$$

As an example, Table S6 reports the separate contributions computed along the MD trajectory for the solvated PDI dimer.

Table S6: Kinetic, potential, and pressure–volume contributions (kJ mol^{-1}) to the stepwise aggregation enthalpy of the PDI dimer.

$\Delta H_{\text{aggr}}^{(S_{1;M} \to S_2)}$	$\Delta E_{\text{aggr}}^{\text{kin},(S_{1;M} \to S_2)}$	$\Delta E_{\text{aggr}}^{\text{pot},(S_{1;M} \to S_2)}$	$\Delta(pV)_{\text{aggr}}^{(S_{1;M} \to S_2)}$
40 ± 32	18 ± 20	22 ± 12	0 ± 0.0

To disentangle intra-stack and solvent effects, the potential energy of each state $Y \in \{S_{N+1}, S_{N;M}\}$ was partitioned into

$$E^{\text{pot}}(Y) = E^{\text{PDI}-\text{PDI}}(Y) + E^{\text{wat}-\text{wat}}(Y) + E^{\text{PDI}-\text{wat}}(Y). \tag{S5}$$

Accordingly, the stepwise differences for the PDI–PDI and wat–wat contributions were directly computed as

$$\Delta E_{\text{aggr}}^{\text{PDI}-\text{PDI},(S_{N;M}\to S_{N+1})} = \left\langle E^{\text{PDI}-\text{PDI}}(S_{N+1})\right\rangle - \left\langle E^{\text{PDI}-\text{PDI}}(S_{N;M})\right\rangle$$

$$\Delta E_{\text{aggr}}^{\text{wat}-\text{wat},(S_{N;M}\to S_{N+1})} = \left\langle E^{\text{wat}-\text{wat}}(S_{N+1})\right\rangle - \left\langle E^{\text{wat}-\text{wat}}(S_{N;M})\right\rangle, \quad \text{(S6)}$$

The PDI–water term was then obtained by difference as

$$\Delta E_{\text{aggr}}^{\text{PDI}-\text{wat},(S_{N;M}\to S_{N+1})} = \Delta E_{\text{aggr}}^{\text{pot},(S_{N;M}\to S_{N+1})} - \Delta E_{\text{aggr}}^{\text{PDI}-\text{PDI},(S_{N;M}\to S_{N+1})} - \Delta E_{\text{aggr}}^{\text{wat}-\text{wat},(S_{N;M}\to S_{N+1})}. \quad \text{(S7)}$$

The resulting values for dimer, tetramer, and hexamer are reported in Table S7.

Table S7: Stepwise contributions (kJ mol^{-1}) to the aggregation energy for PDI aggregates in water.

	$\Delta E_{\text{aggr}}^{\text{pot},(S_{N;M}\to S_{N+1})}$	$\Delta E_{\text{aggr}}^{\text{PDI-PDI},(S_{N;M}\to S_{N+1})}$	$\Delta E_{\text{aggr}}^{\text{wat-wat},(S_{N;M}\to S_{N+1})}$	$\Delta E_{\text{aggr}}^{\text{PDI-wat},(S_{N;M}\to S_{N+1})}$
$PDI_2@H_2O$	22	-47	-19	88
$PDI_4@H_2O$	54	-74	-37	165
$PDI_6@H_2O$	82	-99	-57	238

Both $\Delta E_{\text{aggr}}^{\text{PDI-PDI},(S_{N;M}\to S_{N+1})}$ and $\Delta E_{\text{aggr}}^{\text{wat-wat},(S_{N;M}\to S_{N+1})}$ are negative, indicating that PDI–PDI and H_2O–H_2O interactions favor aggregation. As discussed in the main text, the former includes both π–stacking between the cores and side–chain contacts, which respectively stabilize and destabilize aggregation. The $\Delta E_{\text{aggr}}^{\text{wat-wat},(S_{N;M}\to S_{N+1})}$ contribution arises from the new hydrogen bonds formed among water molecules released from the interplanar region. However, the favorable terms are outweighed by the strongly positive $\Delta E_{\text{aggr}}^{\text{PDI-wat},(S_{N;M}\to S_{N+1})}$, which reflects the reduced hydration of PDI units upon aggregation compared with the monomers in solution.

D.3 Role of Solvation

As shown in the previous section, the solvent interactions established with the PDI units are a determining factor for the sign of ΔE_{aggr} and, consequently, for the aggregation enthalpy, ΔH_{aggr}. In the following a further analysis of the solvent-PDI interactions is presented, taking into account both thermodynamic contributions and the specific role of hydrogen bonds.

Table S8: LJ and Coulomb contribution to the interaction energy ΔE_{kl} between PDI cores *a* and *b*, chains (right-chain$_{a,b}$,left-chain$_{a,b}$) and water molecules computed along the MD simulations of **PDI$_2$**@H_2O.

Pair (k-l)	**LJ (kJ mol^{-1})**	**Coul (kJ mol^{-1})**
core$_a$–wat	-82 ± 10	-83 ± 21.9
core$_b$–wat	-82 ± 10	-84 ± 22
left-chain$_a$–wat	-33 ± 6	-58 ± 14
right-chain$_a$–wat	-33 ± 6	-62 ± 14
left-chain$_b$–wat	-33 ± 6	-57 ± 13
right-chain$_b$–wat	-33 ± 6	-61 ± 14
wat–wat	19036.4 ± 366.0	-139095 ± 587
wat–wat	6.3 ± 0.1	-46.0 ± 0.2

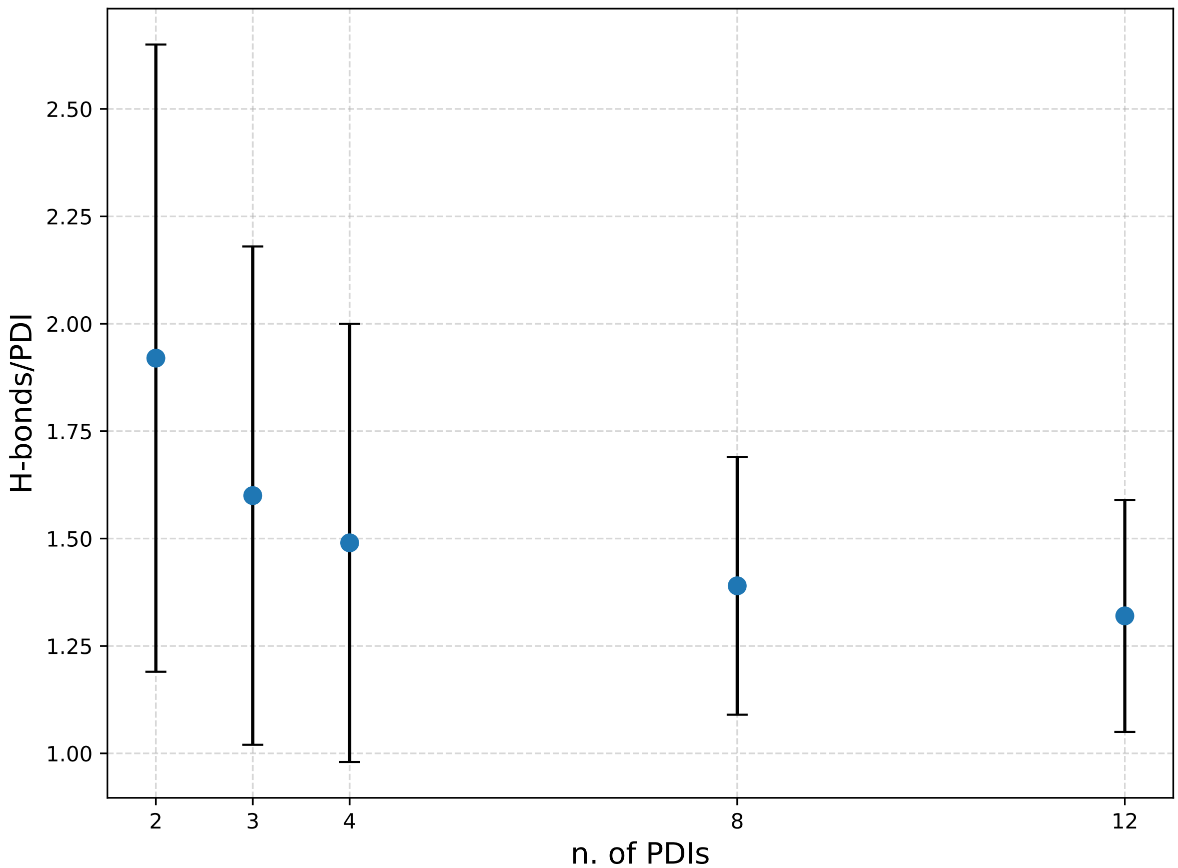

Figure S47: Average number and standard deviation of H-bonds per monomeric unit between the PDIs carbonyl oxygens atoms and the water molecules calculated along the MD trajectory for supramolecular aggregates: $\mathbf{PDI_2}@H_2O$ (n. of PDIs=2), $\mathbf{PDI_3}@H_20$ (n. of PDIs=3), $\mathbf{PDI_4}@H_20$(n. of PDIs=4), $\mathbf{PDI_8}@H_2O$ (n. of PDIs=8) and $\mathbf{PDI_{12}}@H_2O$ (n. of PDIs=12). The cutoff utilized for the donor–acceptor distance is 3.5 Å.

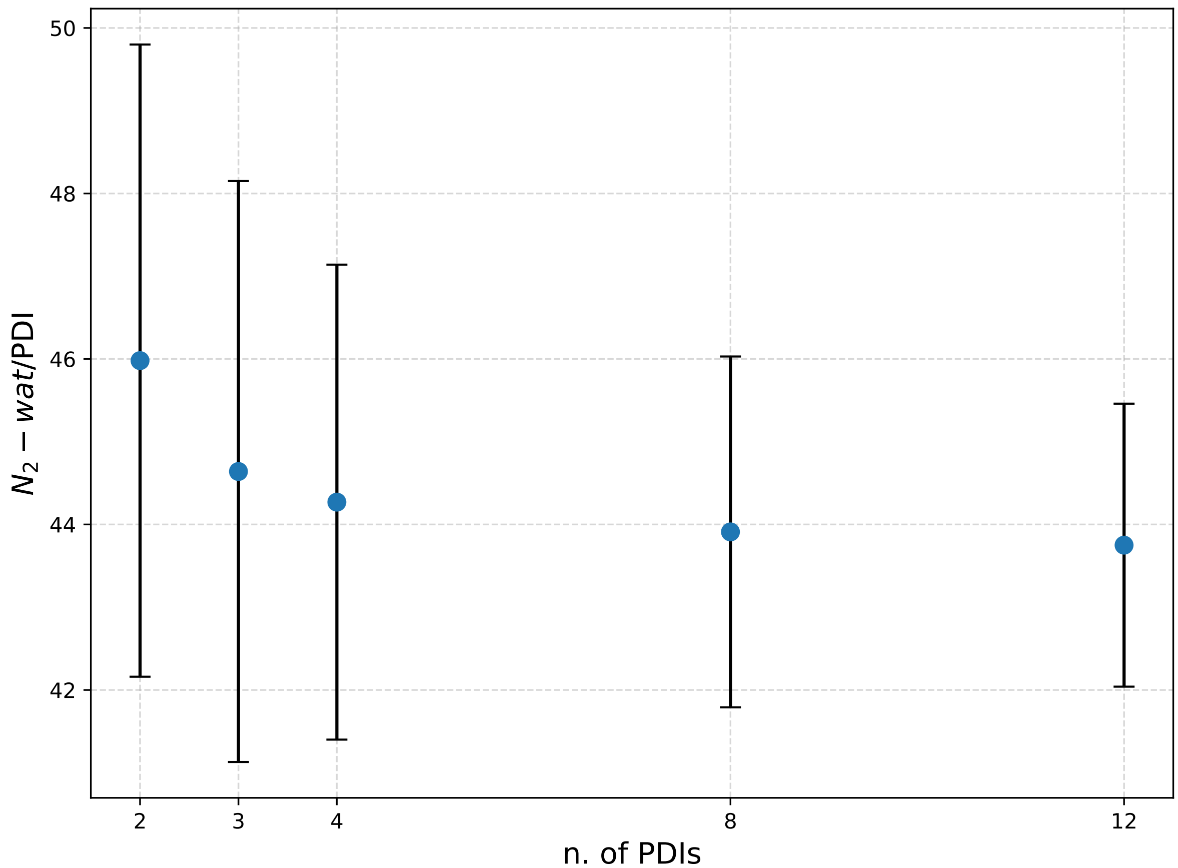

Figure S48: Average number and standard deviation of interactions between the positively charged nitrogen (N_2) from the side chains of PDI and water molecules per monomeric unit, calculated along the MD trajectory for supramolecular aggregates: $\mathbf{PDI_2}@H_2O$ (n. of PDIs=2), $\mathbf{PDI_3}@H_20$ (n. of PDIs=3), $\mathbf{PDI_4}@H_20$(n. of PDIs=4), $\mathbf{PDI_8}@H_2O$ (n. of PDIs=8) and $\mathbf{PDI_{12}}@H_2O$ (n. of PDIs=12). The cutoff utilized for the donor–acceptor distance is 5 Å. (see section C)

D.4 Water counting between PDI planes

To gain mechanistic insight into the aggregation process, we quantified the number of water molecules confined between two PDI cores during the dimer trajectories. This analysis follows how initially hydrated aromatic surfaces progressively force out the solvent from the interplanar region, ultimately yielding an almost dry π–stacked configuration. By monitoring both the population of confined waters and their exit pathways, we obtained direct information on the microscopic mechanism of solvent removal upon self-assembly.

A water molecule was classified as interlayer if its oxygen atom lays between the two PDI planes (slab criterion) and within the lateral footprint of the aromatic cores (footprint criterion). Least-squares planes were fitted through the aromatic atoms of each PDI, yielding centroids $\mathbf{r}_0^{(A)}$, $\mathbf{r}_0^{(B)}$ and unit normals $\hat{\mathbf{n}}_A$, $\hat{\mathbf{n}}_B$. After alignment, a common interplanar axis was defined as

$$\hat{\mathbf{n}} = \frac{\hat{\mathbf{n}}_A + \hat{\mathbf{n}}_B}{|\hat{\mathbf{n}}_A + \hat{\mathbf{n}}_B|}. \tag{S8}$$

The instantaneous interplanar separation was

$$R_\pi = \hat{\mathbf{n}} \cdot \left(\mathbf{r}_0^{(B)} - \mathbf{r}_0^{(A)}\right), \qquad R_\pi > 0. \tag{S9}$$

For each water oxygen at position $\mathbf{r}_i$, the signed height relative to the lower plane was

$$s_i = \hat{\mathbf{n}} \cdot \left(\mathbf{r}_i - \mathbf{r}_0^{(A)}\right), \tag{S10}$$

and the slab criterion required

$$0 < s_i < R_\pi. \tag{S11}$$

To test whether a water lies within the lateral footprint of the PDI stack, each oxygen position $\mathbf{r}_i$ was projected onto the dimer midplane by subtracting its out-of-plane component $s_i\hat{\mathbf{n}}$:

$$\mathbf{p}_i = \mathbf{r}_i - s_i\hat{\mathbf{n}}. \tag{S12}$$

Here, $\mathbf{p}_i$ is the two-dimensional in-plane coordinate of the water, while s_i (already defined) measures how far the molecule sits along the interplanar axis. The aromatic atoms of both PDI cores were projected in the same way, and their in-plane coordinates were used to construct the convex hull, i.e., the minimal convex polygon enclosing all core atoms. This hull defines the effective lateral footprint of the stacked aromatic surfaces. A water molecule was considered inside the footprint if its projection $\mathbf{p}_i$ lays within this convex hull (with a small tolerance parameter for numerical stability), as tested by the indicator function $\chi_{\text{lat}}(\mathbf{p}_i) \in \{0,1\}$, which returns 1 for inclusion and 0 otherwise.

In this way, only molecules that simultaneously satisfy the slab condition ($0 < s_i < R_\pi$) and the footprint condition are counted as within the interlayer region. To make this explicit, we defined a combined indicator function

$$\chi_{\text{conf}}(\mathbf{r}_i) = \begin{cases} 1, & 0 < s_i < R_\pi \ \text{ and } \ \mathbf{p}_i \in \text{hull}, \\ 0, & \text{otherwise}, \end{cases} \tag{S13}$$

so that the instantaneous number of confined waters reads simply

$$N_{\text{w}} = \sum_i \chi_{\text{conf}}(\mathbf{r}_i). \tag{S14}$$

Both R_π and N_{w} were monitored throughout the trajectories, and the coordinates of waters crossing either the slab boundaries ($s_i = 0$ or $s_i = R_\pi$) or the hull rim were logged to construct exit maps. This procedure provided a microscopic picture of how interfacial waters are displaced from the interplanar region, offering direct mechanistic clues on the solvent-expulsion process that drives π–stack formation.